Thermo-hydraulic characteristic investigation of a circular tube inserted with constructal bifurcation semi-pipes by numerical simulation and PIV experiments

Qinglin Du [a], Yuhao Zhu [a], Peng Liu [b,*], Zhichun Liu [a], Wei Liu [a,*]

[a] *School of Energy and Power Engineering, Huazhong University of Science and Technology, Wuhan, 430074, China*
[b] *Institute of Thermal Science and Power Engineering, Wuhan Institute of Technology, Wuhan, 430205, China*

ARTICLE INFO

ABSTRACT

Applying longitudinal swirl generators, an efficient approach for heat transfer enhancement, has attracted much attention recently. In this work, a novel type of insert, constructal bifurcation semi-pipes (CBSPs), is proposed in combination with the tree-shaped bifurcation structure extensively used in constructal design, aiming to improve the tube wall's temperature uniformity while generating multiple longitudinal swirling flows in the circular tube. The heat transfer enhancement mechanism of CBSPs under laminar flow is investigated through numerical simulation and stereoscopic particle image velocimetry (Stereo-PIV) experiment. The effects of four geometric parameters (slant angle (α), bifurcation angle (β), bifurcation distance (h), and pitch (P)) on the thermo-hydraulic performance of the enhanced tube are explored. The results indicated that compared to previous longitudinal swirl generators CBSPs can improve the tube wall's temperature uniformity. The Nusselt number is increased by 5.35–8.16 times with the friction factor increasing by 4.19–9.41 times compared with the smooth tube. The efficiency evaluation coefficient (*EEC*) reaches a maximum of 1.44. Furthermore, a multi-objective optimization is performed according to the principle of exergy destruction minimization. The geometric parameters of the compromised point on the Pareto front are $\alpha = 30.19°$, $\beta = 53.56°$, h=5.67 mm, P=87.80 mm, and the corresponding *EEC* = 1.35, which proved that the principle of exergy destruction minimization is effective for design and optimization.

1. Introduction

Energy crisis is becoming increasingly serious. For energy-saving, one of the most important approaches is improving energy utilization efficiency, of which the key is to modify heat transfer equipment. According to the requirement of external power, the heat transfer enhancement techniques can be divided into active techniques, passive techniques and compound enhancements which use two or more heat transfer enhancement techniques together [1,2]. Active techniques [3,4] and compound enhancements [5,6] have high system complexity and thus limit their industrial applications. Passive techniques are widely applied in industry because of their lower system complexity, lower cost and high reliability.

In the development history of passive techniques, some researchers modified the tube wall to increase the heat transfer area and destroy the heat transfer boundary layer. Wang et al. [7] proposed a tube with ellipsoidal dimples and analyzed its thermo-hydraulic performance through experiments. Their experiment results showed that the ellipsoidal dimple structure could accelerate the transition from laminar to turbulent flow and its critical Reynolds number is less than 1000. Compared to smooth tubes, the Nusselt number and friction factor of tube with spherical dimples increased by 34.1–158 % and 32.9–92 %, respectively, while the tube with ellipsoidal dimples got higher performance: the Nusselt number and friction factor were improved by 38.6 %−175.1 % and 26.9 %−75 %, respectively.

However, modifying the tube wall will cause difficulties in manufacture and installation. From the perspective of disturbing the flow, researchers proposed a variety of inserts in the tube. The advantages of inserts are that they can be directly inserted into old tubes to enhance heat transfer and are simple to manufacture, repair and replace. Common inserts are twisted tapes [8,9], coiled wires [10,11], porous media [12,13], etc.

Altun et al. [14] analyzed the comprehensive performance of tubes

Nomenclature

a	side length of the central rod, mm
c_p	specific heat capacity of water, J/(kg·K)
D	inner diameter of the tube, mm
$E_{xd,\Delta T}$	exergy destruction of heat transfer, W
$E_{xd,\Delta p}$	exergy destruction of fluid flow, W
$E_{xd,\Delta T,0}$	exergy destruction of heat transfer in the smooth tube, W
$E_{xd,\Delta p,0}$	exergy destruction of fluid flow in the smooth tube, W
f	friction factor
f_0	friction factor of the smooth tube
h	bifurcation distance of CBSPs, mm
h_0	actual bifurcation distance of CBSPs, mm
h_t	convective heat transfer coefficient, W/(m²·K)
L	length of the tube, mm
L_c	length of the calculation section, mm
l	radial length of CBSPs, mm
Nu	Nusselt number
Nu_0	Nusselt number of the smooth tube
P	pitch of CBSPs, mm
p	pressure, Pa
q	heat flux, W/m²
Re	Reynolds number
T	temperature, K
T_0	environment temperature, K
T_w	average wall temperature K

T_m	average working medium temperature, K
T_{in}	working medium temperature at the inlet, K
u_m	average velocity of fluid, m/s
u_{in}	velocity at the inlet, m/s
u, v, w	velocity components
x, y, z	coordinate axis

Greek symbols

α	slant angle of CBSPs,
β	bifurcation angle of CBSPs,
β_0	actual bifurcation angle of CBSPs,
λ	thermal conductivity of water, W/(m·K)
μ	viscosity of water, kg/(m·s)
ρ	density of water, kg/m³

Abbreviation

ANN	artificial neural network
CBSPs	constructal bifurcation semi-pipes
CFD	computational fluid dynamics
EEC	efficiency evaluation coefficien
MSE	mean square error
NSGA-II	non-dominated sorting genetic algorithm-II
R²	square of regression coefficient
Stereo-PIV	stereoscopic particle image velocimetry;
TOPSIS	technique for order preference by similarity to an ideal solution

inserted with trapezoidal and twisted trapezoidal tapes by experiments under turbulent flow. The result indicated that the heat transfer enhancement caused by twisted trapezoidal tapes is better than that of trapezoidal tapes. The enhanced tube inserted with twisted trapezoidal tapes achieved a peak Nusselt number of 118.46, which represents an improvement factor of 1.57 and 1.9 when compared to twisted tapes and plain tubes, respectively. Deshmukh et al. [15,16] experimentally studied the thermo-hydraulic performance of a tube inserted with curved delta wing vortex generators under laminar or turbulent flow respectively. In the enhanced tube, the Nusselt number increased by 5–15.0 times that of the smooth tube with the Reynolds number varying from 250 to 1500. And the Nusselt number increased by 1.3–5.0 times with the Reynolds number varying from 10,000 to 45,000.

Nevertheless, these researches mentioned above mainly considered the heat transfer enhancement according to the first law of thermodynamics. From the perspective of the second law of thermodynamics, scholars proposed numerous heat transfer enhancement theories and thermodynamic quantities such as entropy generation [17], entransy dissipation [18] and exergy destruction [19]. Among them, the exergy destruction in terms of energy unit could easily evaluate the available energy loss caused by the irreversibility. In a thermo-hydraulic system, exergy destruction can be divided into two parts: exergy destruction caused by heat transfer which represents thermal dissipation and exergy destruction caused by fluid flow which represents power consumption. In the latest years, researchers optimized the flow field in circular tubes with different objectives such as exergy destruction [20] while keeping power consumption constant. Multiple longitudinal swirling flows, which could significantly enhance heat transfer while the flow resistance increased little, were found in the optimal flow field, and a series of inserts to generate multiple longitudinal swirling flows were proposed. To improve inserts' effect of guiding the fluid, Lv et al. [21] proposed the center-connected deflector and analyzed its comprehensive performance under the laminar flow by numerical simulation. The results indicated that multiple longitudinal swirling flows appeared in the enhanced tube. Compared with the smooth tube, the Nusselt number of the enhanced tube was increased by 2.51–9.46 times while the

friction factor increasing to 2.48–10.77 times. For turbulent flow, Sun et al. [22] designed multiple rectangular winglet vortex generators as the tube inserts and explored the correlations of its thermo-hydraulic performance through experiment and numerical simulation. Both the experimental and numerical results showed that multiple longitudinal swirling flows were generated in the circular tube and the number of swirling flows were proportional to that of winglets. For the considered Reynolds numbers, the Nusselt number and friction factor ratios for the enhance tube and smooth tube were in range of 1.15–2.32 and 1.46–11.63, respectively.

However, multiple longitudinal swirling flows also lead to high-temperature regions on the tube wall, which may shorten its life and raise safety concerns. In this regard, constructal theory has a guiding role [23,24]. Constructal theory was first proposed by Bejan [25,26], which was derived from various natural structures, such as the bifurcation of tree branches, the bronchial system, etc. These structures could provide more convenient paths for the "flow" in the system. Zahra et al. [27] studied a cylinder with fins based on the constructal theory. The simulation results showed that with constant fin length, increasing the number of fin branches would effectively enhance its heat transfer performance. Yu et al. [28] designed a constructal bifurcation filler according to constructal concept as a substitute for a porous media filler. Compared to a porous media filler with the same porosity, the pressure drop caused by the constructal bifurcation filler reduced notably.

In conclusion, the use of many current longitudinal swirl generators results in local high-temperature regions on the tube wall, where the heat transfer enhancement is relatively poor. Our work aims to address this issue. In this paper, a novel insert, constructal bifurcation semi-pipes (CBSPs), is proposed based on the tree-shaped bifurcation structure extensively used in constructal design. Compared with previous longitudinal swirl generators, CBSPs with the newly added bifurcation structures can guide the fluid to specifically cool down the local high-temperature regions on the tube wall, improve the tube wall's temperature uniformity, and thus further enhance heat transfer. The thermo-hydraulic performance of a tube inserted with CBSPs is investigated through numerical simulation and stereoscopic particle image
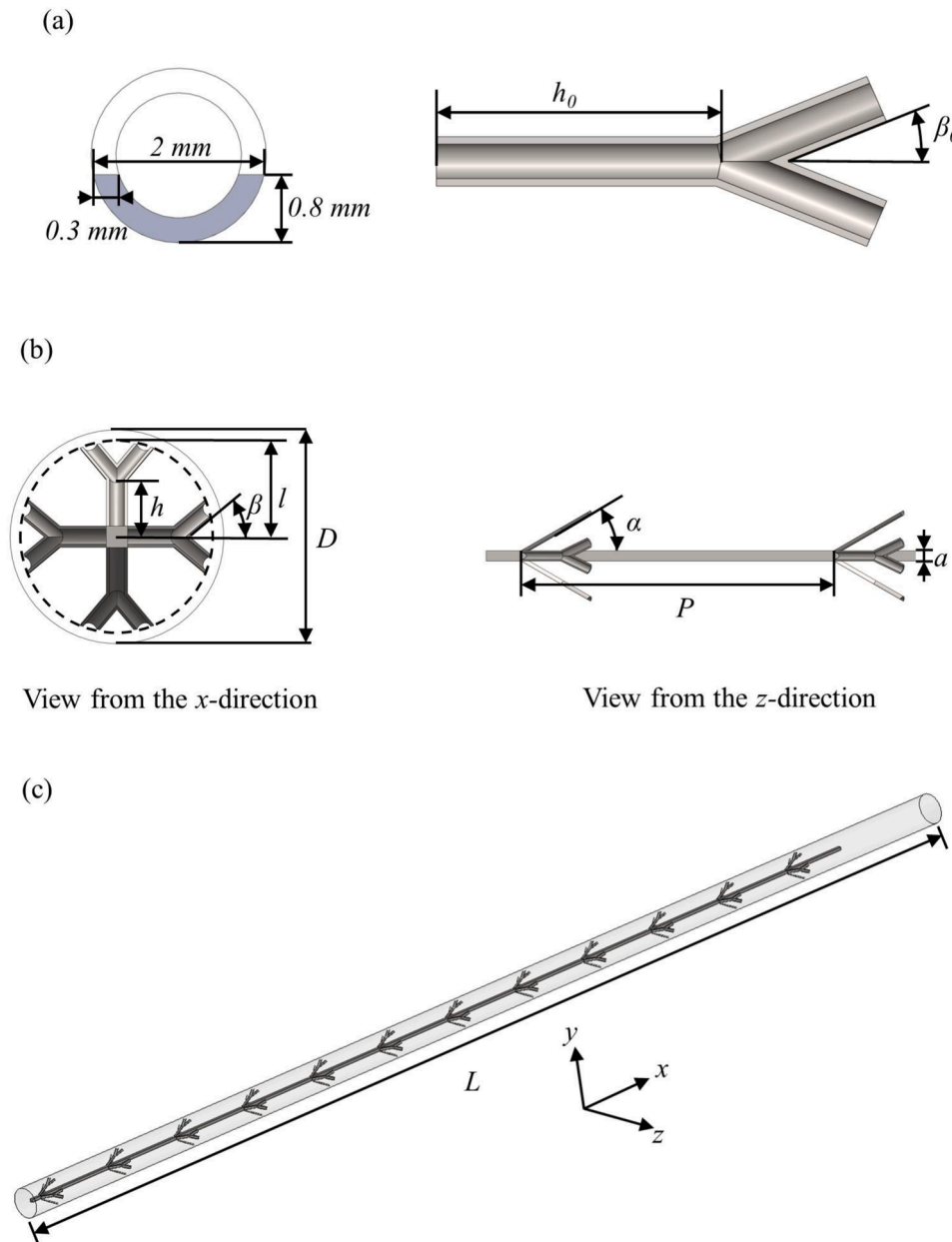
(a)

(b)

(c)

Fig. 1. Geometrical model: (a) constructal structure, (b) constructal bifurcation semi-pipes, and (c) computational domain of the enhanced tube inserted with CBSPs.

Table 1

Geometric parameters of the enhanced tube inserted with CBSPs.

Geometric parameter	Value
length of the tube L, mm	800
inner diameter of the tube D, mm	20
radial length of CBSPs l, mm	9
side length of the central rod a, mm	2
slant angle of CBSPs α, °	30, 40, 50, 60
bifurcation angle of CBSPs β, °	30, 40, 50, 60
bifurcation distance of CBSPs h, mm	5, 5.5, 6, 6.5
pitch of CBSPs P, mm	60, 80, 100, 120

velocimetry (Stereo-PIV) [29,30] experiments. Furthermore, a multi-objective optimization for the parameters of CBSPs is conducted using the non-dominated sorting genetic algorithm-II (NSGA-II) [31,32] along with artificial neural network (ANN) according to the principle of exergy destruction minimization [19].

2. Geometrical model

Fig. 1(a) illustrates the cross-section and global structure of a CBSP unit. It can be observed that the unit is constructed by combining semi-pipes to guide the fluid, which consists of a parent semi-pipe with an actual bifurcation distance (h_0) and two symmetrical sub semi-pipes extending at the end of the parent semi-pipe with an actual bifurcation angle (β_0) like a tree branch growing. The geometrical model of CBSPs is shown in Fig. 1(b). The insert is obtained by arranging CBSP units with equal spacing and circumferential symmetry at a slant angle (α) to the central rod. When observed from the x-direction, bifurcation angle (β) and bifurcation distance (h) represent the projections of the actual bifurcation angle (β_0) and the actual bifurcation distance (h_0) onto the y-z plane, respectively. These parameters are interconnected through the following geometric relationship:
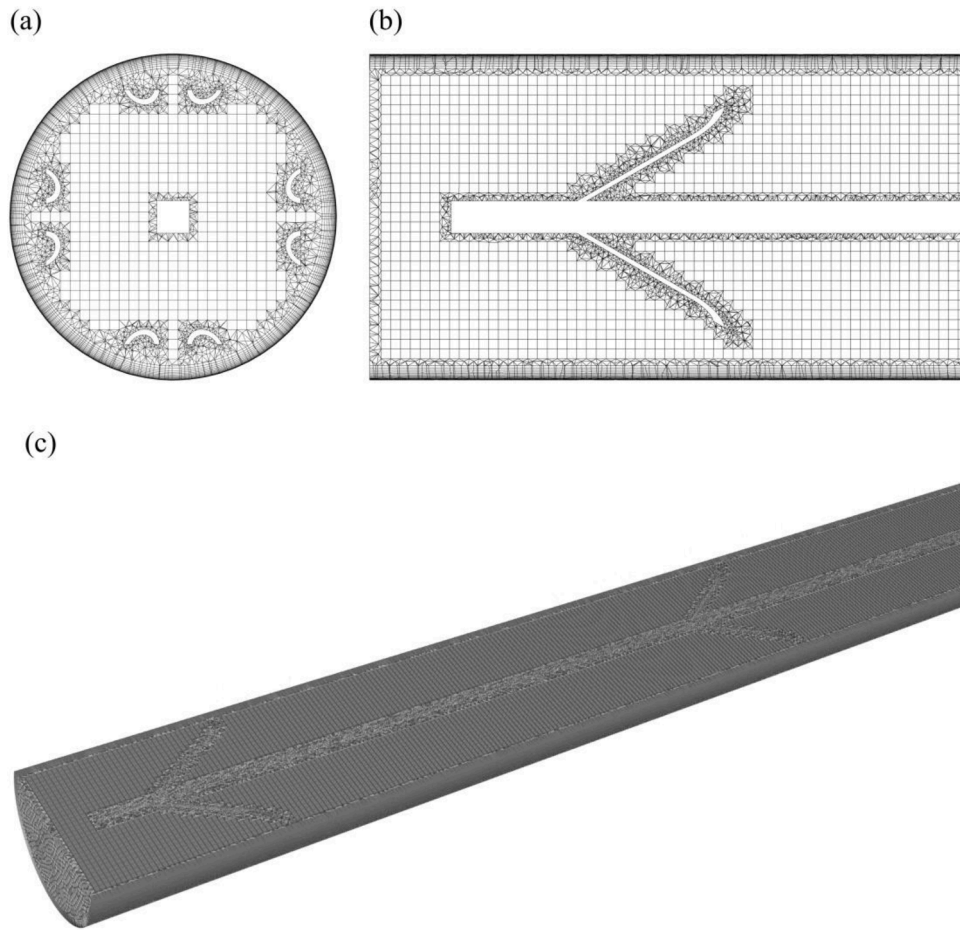
$$\tan\beta\sin\alpha = \tan\beta_0 \tag{1}$$

Fig. 2. Grid system: (a) *y-z* plane, (b) *x-y* plane and (c) 3D shape.

Table 2
Grid independence test.

Grid numbers	Nu/Nu_0	Deviation of Nu/Nu_0	f/f_0	Deviation of f/f_0
2730,000	6.84	–	5.18	–
5730,000	7.12	4.09 %	5.35	3.28 %
11,750,000	7.34	3.09 %	5.48	2.43 %
19,210,000	7.40	0.82 %	5.52	0.73 %

$$h = h_0 \sin\alpha \tag{2}$$

For convenience, β and h are selected instead of β_0 and h_0 to describe the geometrical model.

The computational domain of a tube inserted with CBSPs is shown in Fig. 1(c). The tube length (L) of 800 mm is sufficient to fully capture the flow field properties. The radial length (*l*) of CBSPs is 9 mm while the tube's inner diameter (*D*) is 20 mm, so that the flow can be fully disturbed. According to the experience of previous studies, the pitch (*P*) and slant angle (*α*) are geometric parameters with greater influences on the thermo-hydraulic performance of the enhanced tube. The bifurcation angle (*β*) and bifurcation distance (*h*) are important geometric parameters for a constructal structure. Therefore, this work will focus on how these four geometric parameters influence the performance. Drawing upon the past experience, a slant angle range of 30–60°, within which the inserts offer greater heat transfer enhancement, is chosen. Given the intricate structure of the CBSPs, we opted for a larger pitch range of 60–120 mm to counterbalance the increase in flow resistance. To prevent excessive distortion of the CBSPs' shape, the ranges of 30–60° and 5–6.5 mm are selected for bifurcation angle and bifurcation

distance, respectively. For each of the above parameters, four values are selected for numerical simulations. Through the full factorial design, a total of 256 cases are analyzed in the numerical simulations. Detailed geometric parameters are listed in Table 1.

3. Numerical simulation

3.1. Simulation parameters

The Reynolds number (*Re*) is defined as:

$$Re = \frac{\rho u_m D}{\mu} \tag{3}$$

where ρ, u_m and μ are the density, mean velocity and dynamic viscosity of the working medium, respectively. Given the sparse distribution of inserts within the tube, attributable to the larger pitch, the internal diameter of the tube is used as an approximation for the hydraulic diameter.

The heat transfer coefficient (h_t) is calculated by:

$$h_t = \frac{q}{T_w - T_m} \tag{4}$$

where q is the heat flux through the tube wall, T_w and T_m are the average wall temperature and average working medium temperature, respectively.

In this paper, the Nusselt number and friction factor are selected to indicate the heat transfer and fluid flow performance of the enhanced tube, which are given by:
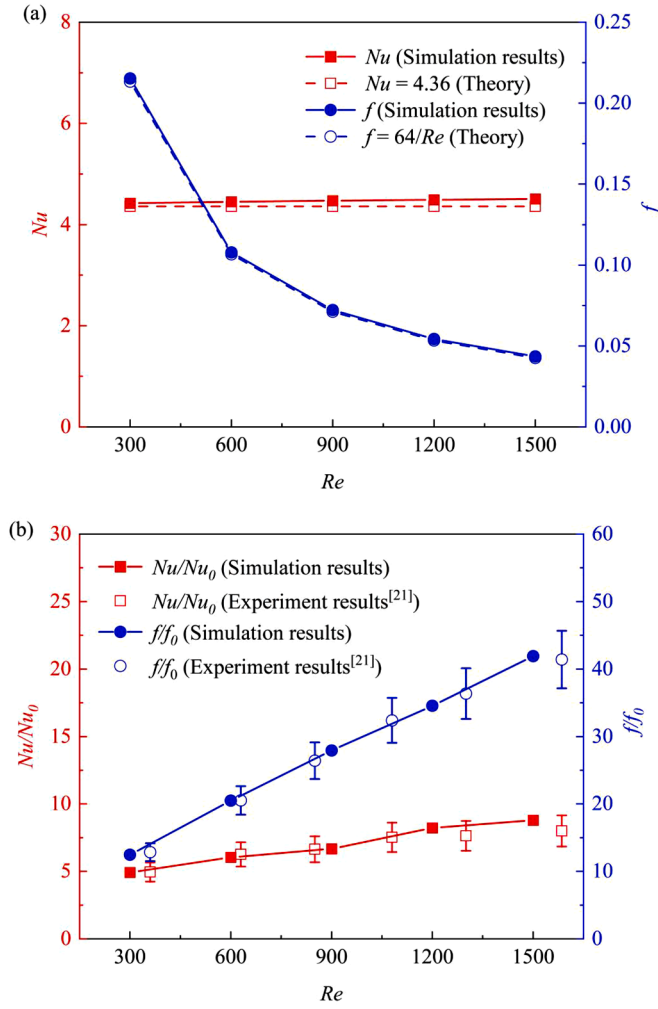
Fig. 3. Validation of numerical model: (a) comparisons between the simulation results and theory for a smooth tube and (b) comparisons between the results of simulation and experiment for the tube inserted with curved delta wings.

$$Nu = \frac{h_t D}{\lambda} \qquad (5)$$

$$f = \frac{\Delta p}{\left(\frac{1}{2}\rho u^2\right)(L_c/D)} \qquad (6)$$

where λ is the heat conductivity coefficient of the working medium, L_c and Δp are the length of the calculation section and the corresponding pressure drop, respectively.

The efficiency evaluation criterion (*EEC*) [19] is selected to evaluate the comprehensive performance of the enhanced tube, which is defined as:

$$EEC = \frac{Nu/Nu_0}{f/f_0} \qquad (7)$$

where Nu_0 and f_0 are the Nusselt number and friction factor of the smooth circular tube with same size and Reynolds number, respectively.

Exergy destruction [19] caused by temperature difference and pressure drop respectively are selected to evaluate the irreversibility for heat transfer and fluid flow, which are given as:

$$E_{xd,\Delta T} = \int\int\int_\Omega T_0 \frac{\lambda(\nabla T)^2}{T^2} dV \qquad (8)$$

$$E_{xd,\Delta p} = \int\int\int_\Omega U \cdot \left(\rho U \cdot \nabla U - \mu \nabla^2 U\right) dV \qquad (9)$$

3.2. Governing equations and boundary conditions

In this work, the selected working medium is liquid water. Considering the limited computational resources, the following assumptions are made in the numerical simulation: (I) liquid water is continuous, Newtonian and incompressible fluid with constant physical properties ($\lambda = 0.6$ W/(m·K), $c_p = 4182$ J/(kg·K), $\mu = 1.003 \times 10^{-3}$ kg/(m·s), $\rho = 998.2$ kg/m^3); (II) CBSPs and the tube are rigid bodies; (III) the thermal conductivity of the insert is ignored; (IV) the influences of thermal radiation and gravity are ignored.

At the inlet, temperature and velocity are uniform ($T_{in} = 300$ K, $u_{in} = 0.045$ m/s, $Re = 900$). The tube wall is no-slip with a constant and uniform heat flux ($q = 2000$ W/m^2). The insert is no-slip and adiabatic.
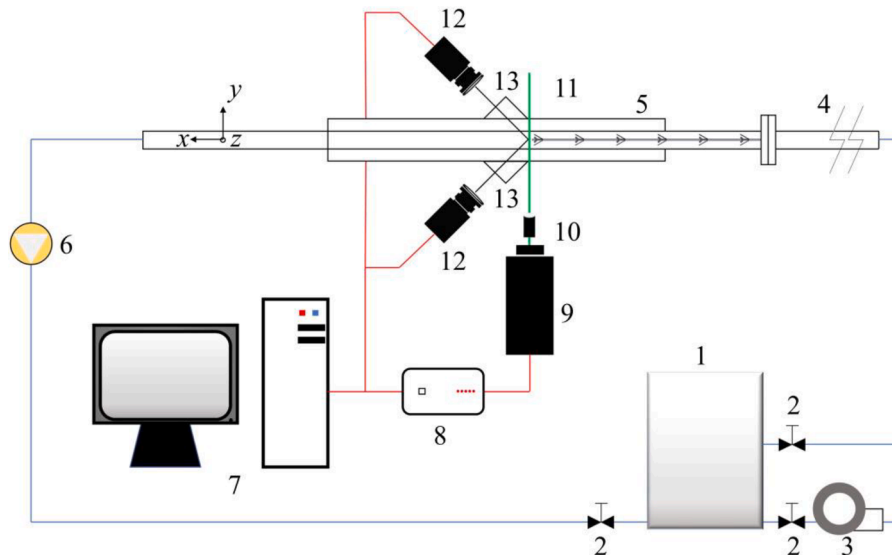

Fig. 4. The schematic diagram of the Stereo-PIV system: 1. water tank, 2. valves, 3. water pump, 4. upstream tube, 5. test section, 6. electromagnetic flowmeter, 7. computer, 8. synchronizer, 9. laser, 10. lenses, 11. light sheet, 12. CCD cameras, 13. water prisms.

Fig. 5. The physical diagram of the Stereo-PIV system.

At the outlet, the "outflow" condition is applied.

The governing equations of continuity, momentum and energy are given as follows:

$$\frac{\partial u_i}{\partial x_i} = 0 (i = 1 \sim 3) \tag{10}$$

$$\frac{\partial}{\partial x_j}(\rho u_i u_j) = -\frac{\partial p}{\partial x_i} + \frac{\partial}{\partial x_j}\left[\mu\left(\frac{\partial u_i}{\partial x_j} + \frac{\partial u_j}{\partial x_i}\right)\right](j = 1 \sim 3) \tag{11}$$

$$\frac{\partial}{\partial x_i}\left(\rho u_i c_p T - \lambda \frac{\partial T}{\partial x_i}\right) = 0 (i = 1 \sim 3) \tag{12}$$

The numerical simulation is run on the commercial software ANSYS Fluent. The Laminar model is chosen as the viscous model and the SIMPLE algorithm is used to solve the velocity and pressure coupled fields. Second Order format is selected for the spatial discretization of pressure and Second Order Upwind format is selected for that of momentum and energy. The calculation can be considered converged when the relative residuals are decreased to 10^{-8} for energy equation and 10^{-6} for continuity equation and those velocity component equations.

3.3. Grid generation

A hybrid unstructured meshing method is adopted to generate a grid system. As shown in Fig. 2, this grid system includes hexahedron grids, tetrahedron grids, prism grids and pyramid grids. To accurately simulate heat transfer and flow phenomena in the boundary layer, prism grids are used near the tube wall, which become finer as they get closer to the wall. High-quality hexahedron grids are applied in the center area of the flow field. Tetrahedron grids and pyramid grids distribute between the various grids as the connecting layers.

In order to eradicate the effect of grid size on the numerical simulation, four systems of different grid sizes are designed for the enhanced tube with selected insert ($\alpha = 30°$, $\beta = 40°$, $h = 5.5$ mm, $P = 80$ mm) and their grid numbers are 2730,000, 5730,000, 11,750,000 and 19,210,000 respectively. Numerical simulations are conducted on the above four models as grid independence verification. Table 2 lists these results. It can be observed when the number of grids increases from 11,750,000 to 19,210,000, the change in the numerical simulation results is less than one percent. This suggests that further densification of the grid beyond

this point has a minimal impact on the results. The accuracy of the grid system with 11,750,000 grids can meet the demand.

3.4. Validation of numerical model

To verify the accuracy of the numerical model, a smooth tube and a tube with curved delta wings ($p/pl = 4.2$, $b/d=1.0$, $\alpha = 45°$) in literature [21] are modeled, and the Nusselt number and friction factor are calculated using the same numerical methods. Fig. 3(a) and (b) reveal the comparisons of the simulation results with the theoretical and experimental values, respectively. The simulation results match well with theoretical and experimental values. The maximum deviation of the Nusselt number and friction factor with theory are 3.3 % and 2.2 % respectively. And that maximum deviation with experiments are 11.7 % and 9.5 % respectively while the experimental errors of Nusselt number and friction factor in the literature are 14.4 % and 10.3 % respectively. Thus, the numerical model used in this work can be considered accurate enough.

4. Experimental setup

In order to verify that the expected flow structure is indeed generated in the enhanced tube and to compare it with the numerical results, the flow field inside the enhanced tube is measured using Stereo-PIV experiments as a qualitative validation. Stereo-PIV is an optical technique of flow visualization which measures the velocity field of an entire region within the flow simultaneously. It is a non-contact method that provides accurate data. The Stereo-PIV process consists of the following steps: first, tracer particles are seeded into the fluid; second, a 532 nm laser illuminates the measured region; third, CCD cameras capture two or more consecutive images of the particle motion; fourth, the velocity vectors at each point are calculated from the particle images using a correlation algorithm. As for the experimental mechanism of Stereo-PIV, please refer to C. W. H. van Doorne [29].

Fig. 4 reveals the schematic diagram of the experiment system, with a red line indicating the measurement system and a blue line indicating the water loop. Fig. 5 shows the corresponding physical diagram. The water loop consists of an upstream tube, a test section, a water tank, a water pump, valves and an electromagnetic flowmeter. The measurement system comprises a computer, a synchronizer, a laser, lenses, CCD
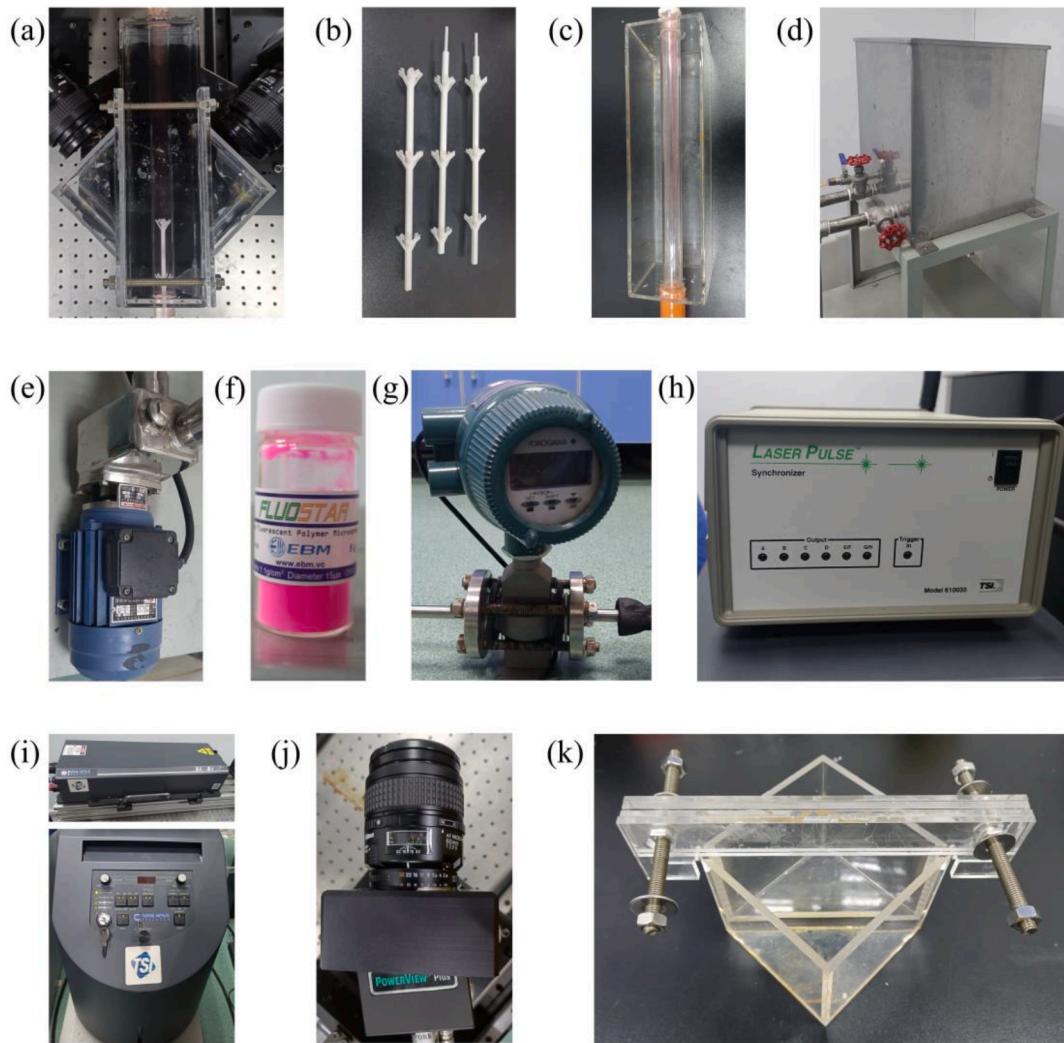
Fig. 6. Test section and relevant experimental devices: (a) test section, (b) CBSPs, (c) water box with a central circular tube, (d) water tank, (e) water pump, (f) electromagnetic flowmeter, (g) tracer particles, (h) synchronizer, (i) laser, (j) CCD camera, and (k) water prisms.

Table 3

The relevant parameters of the Stereo-PIV experiments.

Upstream tube	inner diameter	20 mm
	length	2.5 m
Test section	inner diameter	20 mm
	thickness	2 mm
Tracer particle	type	hollow glass bead
	density	1.1 g/cm^3
	diameter	12 μm
CBSPs	slant angle α	30°
	bifurcation angle β	60°
	bifurcation distance h	6.0 mm
	pitch P	60 mm
Test surface	location	10 mm, 5 mm downstream from the insert

cameras and water prisms.

To prevent rusting in the water tank and pipeline, distilled water has been selected as the working fluid. Hollow glass beads with a density of 1.1 g/cm^3, which is close to that of water and can stay suspended in distilled water for a long time with good tracing performance, are chosen as the tracer particles. A centrifugal pump drives the water loop and several valves and bypasses regulate its flow rate, corresponding to a Reynolds number of 900 measured by an electromagnetic flowmeter. The entire tube's inner diameter is 20 mm, which is consistent with the numerical simulation. The test section for measurement includes CBSPs and a water box with a central circular tube, as shown in Fig. 6(a). In the experiment, the CBSPs with geometric parameters of $\alpha = 30°$, $\beta = 60°$, $h = 6.0$ mm, $P = 60$ mm are selected for the measurements. The inserts are made by resin applying 3D printing and processed in three parts for convenience. Part of the inserts' radial length is 10 mm which equals the tube's inner diameter, thus the inserts can be fixed in the tube by the frictional force. Fig. 6(b) shows the geometrical model of the inserts used in the experiment. The water box and the center circular tube are made of quartz glass which has excellent light transmission. A sufficiently long tube of 2.5 m upstream from the test section ensures flow development. To fully observe the flow structure in the tube, the test surfaces are 10 mm and 5 mm downstream from the insert respectively. Fig. 6 reveals the physical diagram of test section and relevant devices in the Stereo-PIV experiment.

The detailed parameters of the CCD cameras and settings of the software are consistent with Liu's [33]. For both test surfaces, 500 pairs of photos are captured to calculate the vector field. After confirming that all the vector fields from every pairs of photos are basically the same, an average vector field is selected as the final result. The relevant parameters of the Stereo-PIV experiments are listed in Table 3.

5. Results and discussion

5.1. Heat transfer enhancement mechanism

To investigate how CBSPs enhances heat transfer, we compare the temperature field and flow structure of a tube inserted with CBSPs ($\alpha = 30°$, $\beta = 60°$, $h = 5.0$ mm, $P = 60$ mm) and a tube inserted with semi-pipes (with similar geometric parameters). Fig. 7 shows the geometrical models of the tube inserted with CBSPs and the tube inserted with semi-pipes.

The tangential velocity vectors of both enhanced tubes at various cross-sections are compared in Fig. 8. As shown in Fig. 8(a), after flowing through both inserts, the fluid is guided towards the tube wall. As shown in Fig. 8(b), the variation of tangential velocity vectors on different y-z planes indicates how the constructal structure disturbs the flow field. At $x = 15$ mm, the flow structures in both enhanced tubes are approximately the same. At $x = 20$ mm, due to the constructal structure, fluid in the tube inserted with CBSPs is guided in different directions from that in the other tube. At $x = 25$ mm, multiple longitudinal swirling flows are generated with 8 vortexes downstream of semi-pipes and 24 vortexes downstream of CBSPs. It is clear that 4 pairs of large vortexes are formed by parent semi-pipes and 8 pairs of small vortexes are formed by sub semi-pipes in the tube inserted with CBSPs. At $x = 35$ mm, small vortexes gradually merge with the large ones, and at $x = 45$ mm, only 4 pairs of large vortexes remain. Thus, the number of longitudinal swirling flows is eight for both tubes in general. This process can be observed more visually through contours of absolute values of vorticity as shown in Fig. 9. At $x = 25$ mm, large vortexes are circled by red dotted lines and small vortexes by black dotted lines.

Fig. 10 illustrates how the flow structure in enhanced tubes affects the temperature field. As shown in Fig. 10(a), multiple longitudinal swirling flows are generated in the tube inserted with semi-pipes. It can be found that the cold water in the center area flows towards the tube wall, as indicated by the blue lines, while the hot water near the tube wall flows back towards the core region of the tube, as shown by the red lines. The mixing of the cold water from the center area and the hot water near the tube wall within the tube results in the improved temperature uniformity and the enhanced heat transfer. However, the temperature of the tube wall, which does not get directly washed by the cold water, is higher than in other areas. This results in a decline in temperature uniformity along the tube wall, as shown by the red dotted lines in Fig. 10(a). The appearance of high-temperature regions on the tube wall is an inevitable consequence of multiple longitudinal swirling flow structures. To address this issue, a constructal design of bifurcation is applied to the insert. As shown by the black lines in Fig. 10(b), the added sub semi-pipes guide a portion of the cold water from the center area to cool down the high-temperature regions on the tube wall. As a
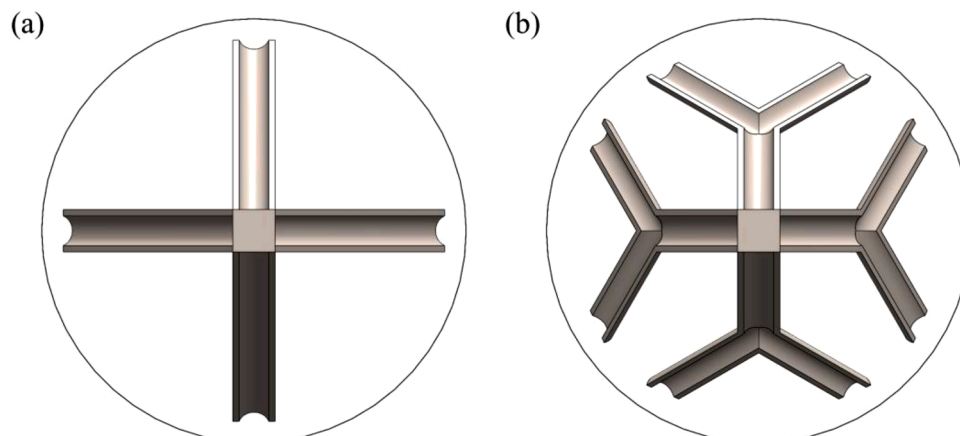

Fig. 7. Geometrical models: (a) the tube inserted with semi-pipes and (b) the tube inserted with CBSPs.
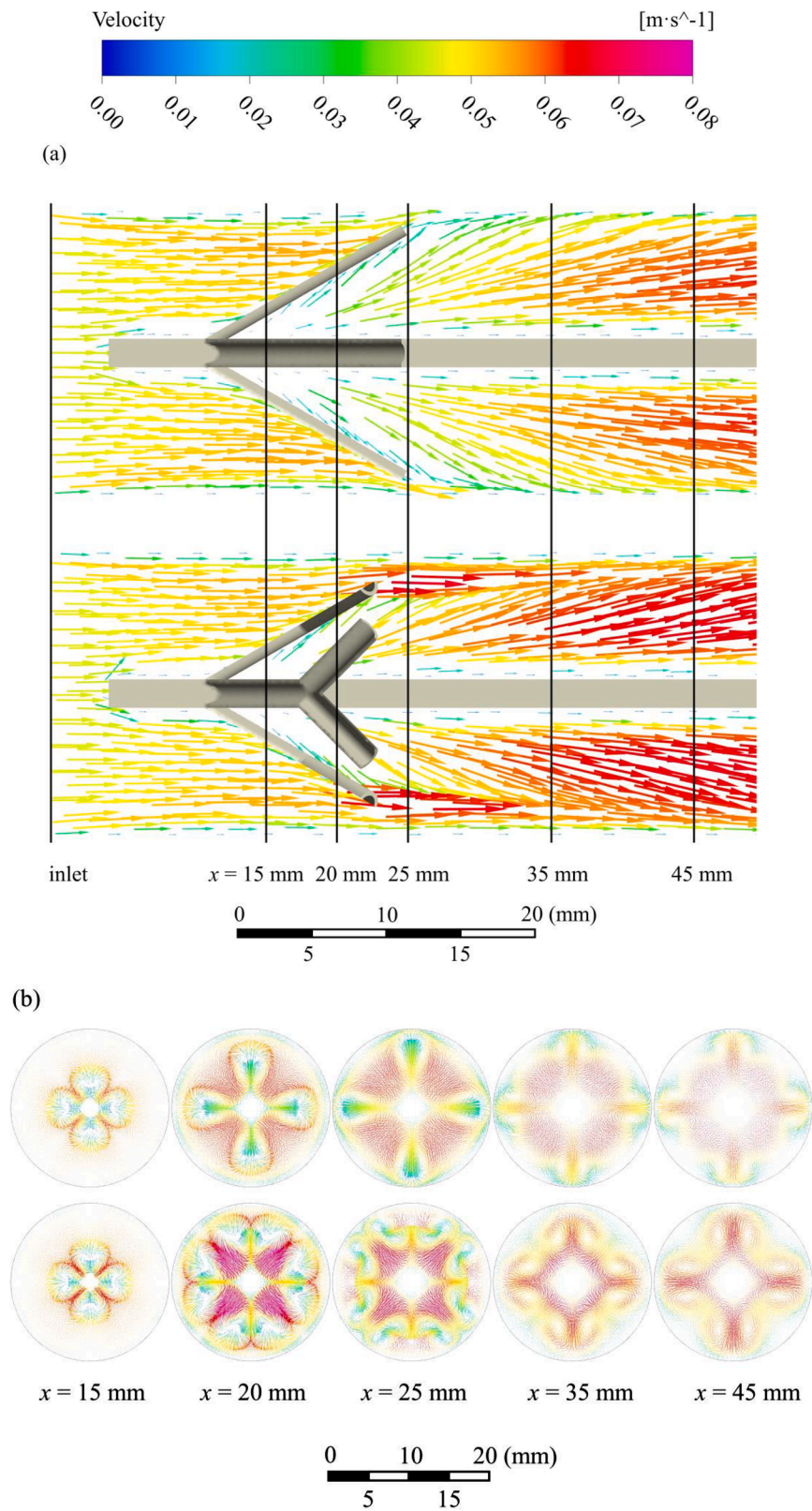
Fig. 8. Tangential velocity vectors of the tube inserted with semi-pipes and the tube inserted with CBSPs: (a) *x-y* plane at *z* = 0 and (b) *y-z* plane.
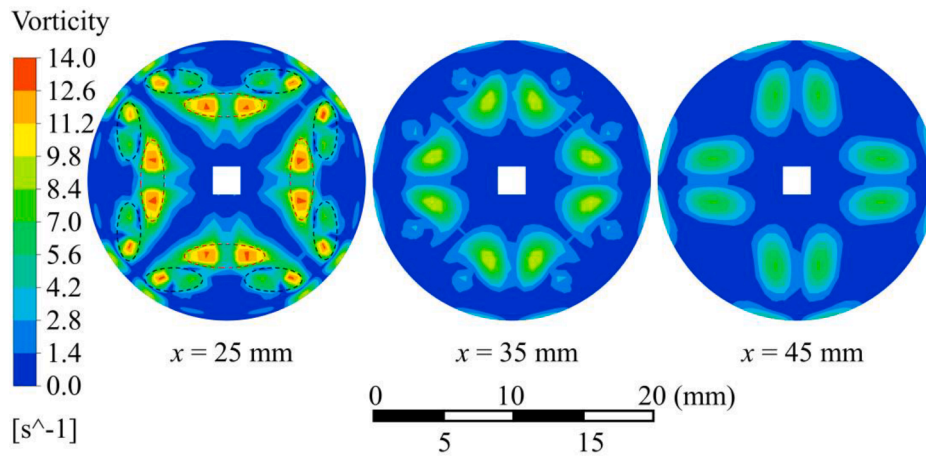
Fig. 9. Contours of absolute value of vorticity in *y-z* plane of the tube inserted with CBSPs.
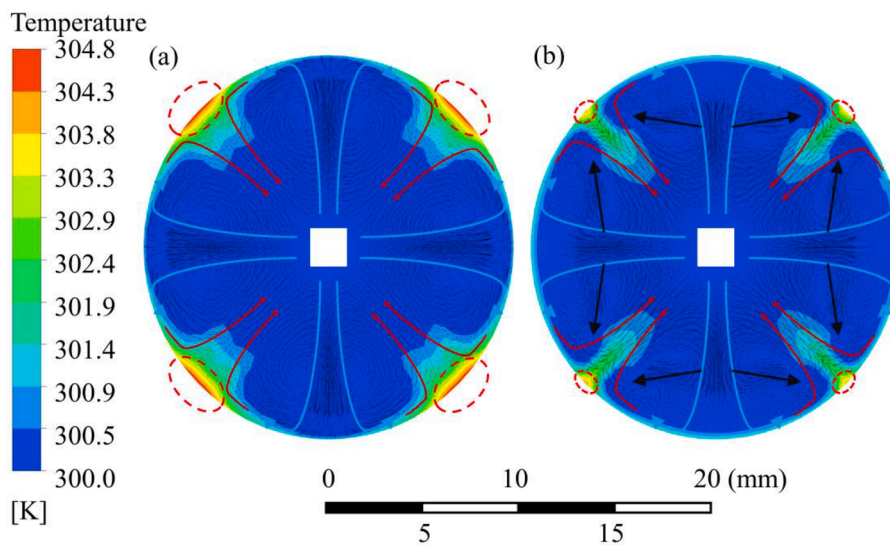

Fig. 10. Temperature contours and tangential velocity vectors in *y-z* plane: (a) the tube inserted with semi-pipes and (b) the tube inserted with CBSPs.

result, the high-temperature area circled by the red dotted lines is significantly reduced, demonstrating that the constructal structure does improve the tube wall's temperature uniformity.

The changes in temperature and flow fields are reflected in the heat transfer performance. As shown in Fig. 11(a), the heat transfer performance along the *x*-axis direction of the enhanced tube reaches stability after the fluid flows through three to four sets of inserts and Nu_x starts to vary periodically with the pitch of the inserts. It can be observed that the heat transfer performance of the tube inserted with semi-pipes is much better than that of the smooth tube, while that of the tube inserted with CBSPs is even better. The Nusselt number of the enhanced tube reaches its highest just after the fluid flows through a set of inserts and then gradually decreases due to the multiple longitudinal swirling flows generated by the inserts downstream of it. To further analyze the heat transfer enhancement caused by these inserts, a cross-section downstream of the fifth set of inserts at *x* = 265 mm, marked with a black dotted line in Fig. 11(a), is selected to analyze the variation in heat transfer performance of the enhanced tube along the circumferential direction.

Considering the symmetry of circular tubes, only the Nu_θ on the upper half of circular tubes is calculated, as shown in Fig. 11(b). It is found that the Nu_θ of the tube with semi-pipes reaches maximum values at 0°, 90° and 180°, which correspond to the regions directly washed by the cold water, and minimum values at 45° and 135°, which correspond

to the high-temperature regions. With the addition of constructal structure to the insert, the Nu_θ distribution of the enhanced tube becomes more uniform. It can be observed that the Nu_θ distribution curve of the tube with CBSPs has more peaks and valleys than that of the tube inserted with semi-pipes. The extra peaks and valleys correspond to areas of the tube wall directly washed by the cold water guided by sub semi-pipes and areas that are not directly washed by the cold water guided by sub semi-pipes, respectively. The Nusselt number is also increased in high-temperature regions. Although the maximum value of Nu_θ for the tube inserted with CBSPs is not as high as for the tube inserted with semi-pipes, the heat transfer performance is on average better.

The heat transfer enhancement mechanism of semi-pipes is mainly due to the generation of multiple longitudinal swirling flows within the tube. This results in a uniform temperature in the core flow region of the tube, thereby enhancing heat transfer. On the other hand, semi-pipes could guide the fluid to wash over the tube wall and break the thermal boundary. However, as mentioned before, this flow field can also cause local high-temperature regions near the tube wall, where the heat transfer enhancement is relatively poor, as shown in Fig. 11(b). Contrastingly, CBSPs add a bifurcation structure based on this, which could guide the fluid to cool down the local high-temperature regions on the tube wall and break the thermal boundary layer more thoroughly. In other words, compared with semi-pipes, CBSPs improve the heat
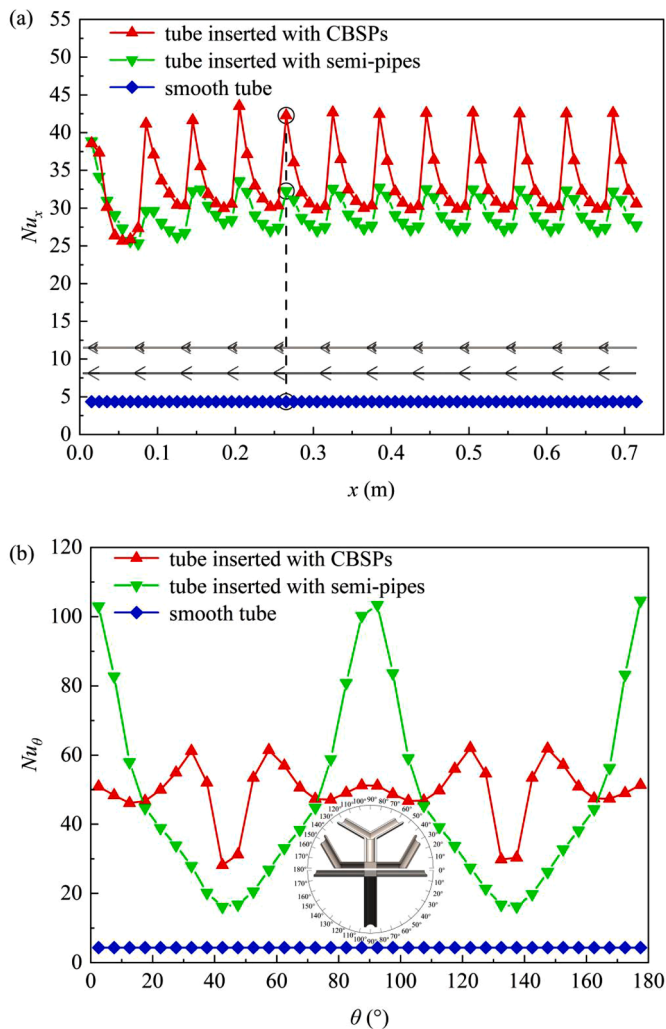
(a)

(b)

Fig. 11. Local Nusselt number of the tube inserted with CBSPs, tube inserted with semi-pipes, and smooth tube: (a) Nu_x along the x-axis direction and (b) Nu_θ along the circumferential direction at $x = 265$ mm.

transfer enhancement near the tube wall. From a quantitative perspective, the enhanced tube inserted with semi-pipes achieved a Nusselt number of 29.21, which is 6.70 times that of a smooth tube. On this basis, CBSPs further enhanced the heat transfer, with the Nusselt number of the enhanced tube reaching 33.25, an increase of 13.8 % compared to semi-pipes, equivalent to 7.63 times that of a smooth tube.

5.2. Experimental results

5.1.1. Uncertainty analysis

To verify the reliability of the experiment results, the Davis 8.3.0 software calculates the uncertainty of the Stereo-PIV experiments by correlation statistics methods [30].

As an example, Fig. 12(a)-(c) shows the velocity contours and the corresponding uncertainties contours in three directions of the test surface 1, respectively. One notable limitation of the PIV experiment is the difficulty in accurately measuring the velocity near the tube wall. As shown in Fig. 12, a minor region near the lower right of the tube wall exhibits significant uncertainty. This is attributed to the sedimentation and accumulation of tracer particles. Disregarding this outlier in the figure, it is evident that the overall relative uncertainty of the velocity is minimal. Furthermore, the relative uncertainty in the x-direction is less than that in the y-direction and z-direction. This is due to the x-direction being the main flow direction with a higher velocity. In accordance with

the principle of PIV experiment, the greater the displacement of a light spot (tracer particles) between two frames, the lesser the uncertainty caused by the light spot's size. This is consistent with the experimental result.

5.1.2. Comparison between the PIV experimental and numerical results

The test surface 1 of the Stereo-PIV experiment is downstream from the insert 10 mm and the simulation result at the same position is compared with it. The comparison for tangential velocity vectors of experiment and simulation results is shown in Fig. 13. Four pairs of vortexes are formed which proves that CBSPs can generate multiple longitudinal swirling flows in the enhanced tube. Moreover, the shapes of the multiple longitudinal swirling flow structure in both results are generally the same. Fig. 14 shows the corresponding vorticity contours and it can be seen that the simulation result is close to the experiment result in terms of magnitude, which further illustrates the reliability of the numerical simulation.

The experimental results from test surface 1 confirm the feasibility of using CBSPs as longitudinal swirl generators. However, the unique flow structure caused by CBSPs has not been verified yet. Therefore, we selected test surface 2 which is 5 mm downstream the insert to observe the real flow field. As before, the simulation result at the same position is compared with it. The comparison for tangential velocity vectors of experiment and simulation results is shown in Fig. 15. Compared with the tangential velocity vectors for test surface 1, it is clear that the shapes of vortexes are different. For test surface 2, it can be observed from both results that part of the fluid are guided to wash over the high-temperature regions on the tube wall. This phenomenon mentioned in the previous subsection caused by the constructal structure is also reproduced in the experiment. The corresponding vorticity contours for test surface 2 are shown in Fig. 16. The experiment result agrees well with that of simulation, both of which reveal the process of the small vortexes caused by the sub semi-pipes merging with the large ones caused by the parent semi-pipes. According to the verification by Stereo-PIV experiments, the analysis of heat transfer enhancement mechanism in this paper is reasonable reliable. The CBSPs insert does generate multiple longitudinal swirling flows in the enhanced tube and guide a portion of the cold water in center area to cool down the high-temperature regions on the tube wall.

5.3. Effects of geometric parameters

5.3.1. Effects of slant angle and pitch

With the bifurcation angle fixed at 40° and the bifurcation distance fixed at 5.5 mm, the thermo-hydraulic performance of enhanced tubes varies with the slant angles under different pitches, as shown in Fig. 17. It is found that the variation of the ratios of the Nusselt number agrees well with that of the exergy destruction of heat transfer and the variation of the ratios of the friction factor agrees well with that of the exergy destruction of fluid flow. This reveals that the evaluation indicators for irreversibility according to the second law of thermodynamics are somewhat consistent with the performance according to the first law of thermodynamics.

From Fig. 17(a), it can be observed that with the increase of α, the Nusselt number of the enhanced tube first increases and then decreases, reaching a maximum at $\alpha = 40°$ This is because as α increases, the cold water guided by CBSPs to cool down the tube wall will have a larger velocity component perpendicular to the wall, but less fluid will be guided. Thus, the fluid washing over the tube wall downstream of the insert will not necessarily have a larger velocity component perpendicular to the wall. It is obvious that the velocity component v in the y-axis direction is perpendicular to the tube wall at $z = 0$ in the x-y plane. The velocity component v of the fluid downstream of the insert first increases and then decreases, reaching a maximum at $\alpha = 40°$, which is consistent the variation pattern of Nu, as shown in Fig. 18(a). The velocity component u in the main flow direction will sharply reduce in
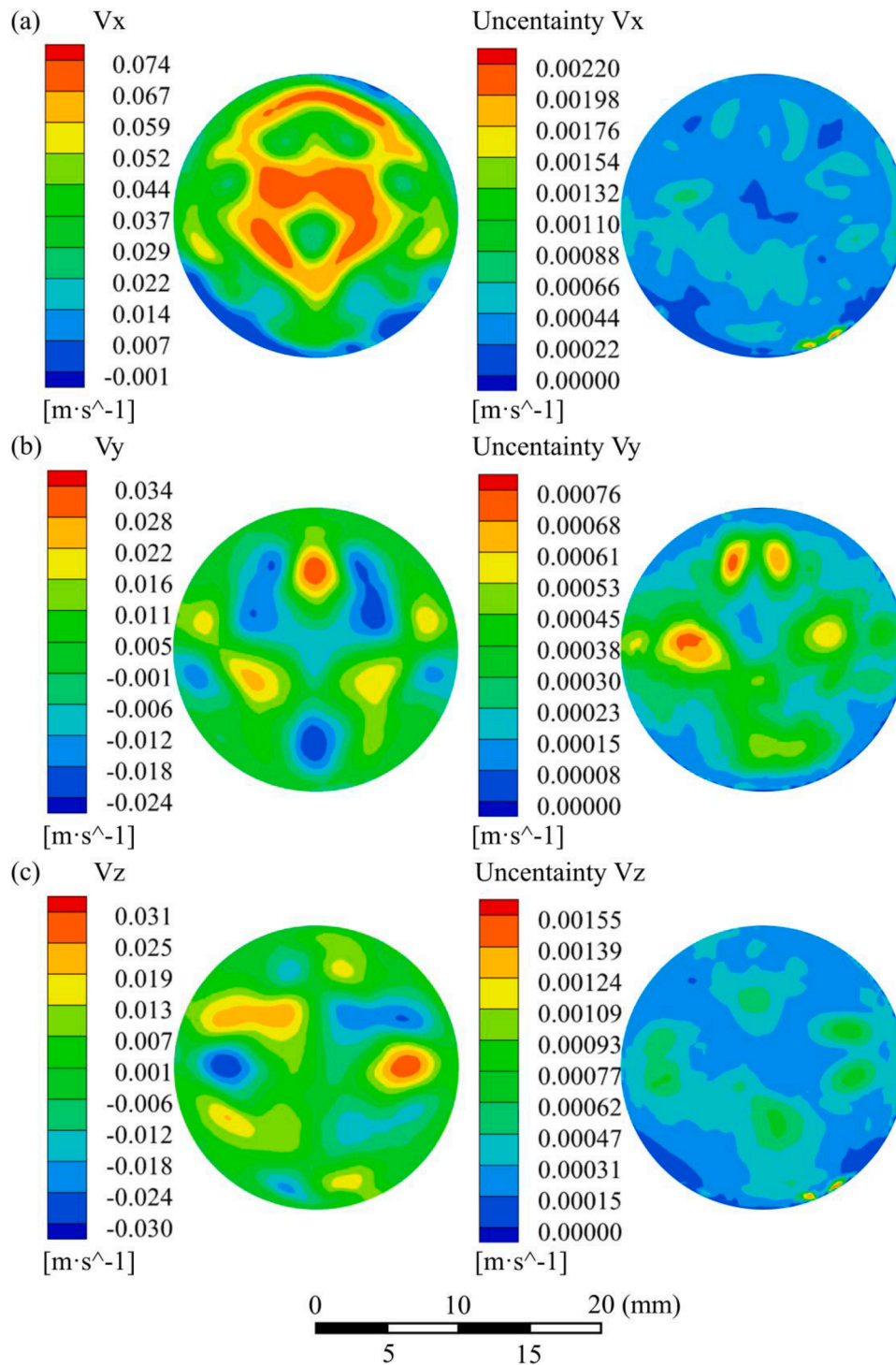
Fig. 12. The contours of velocities and uncertainties in the Stereo-PIV experiment: (a) *x*-direction, (b) *y*-direction and (c) *z*-direction.
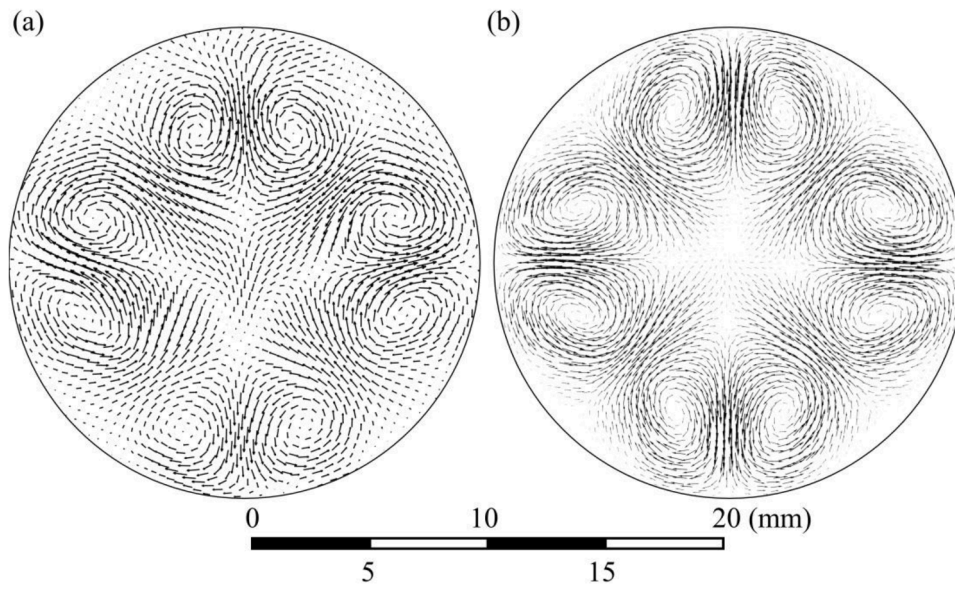
Fig. 13. Tangential velocity vectors for test surface 1: (a) experiment result and (b) simulation result.
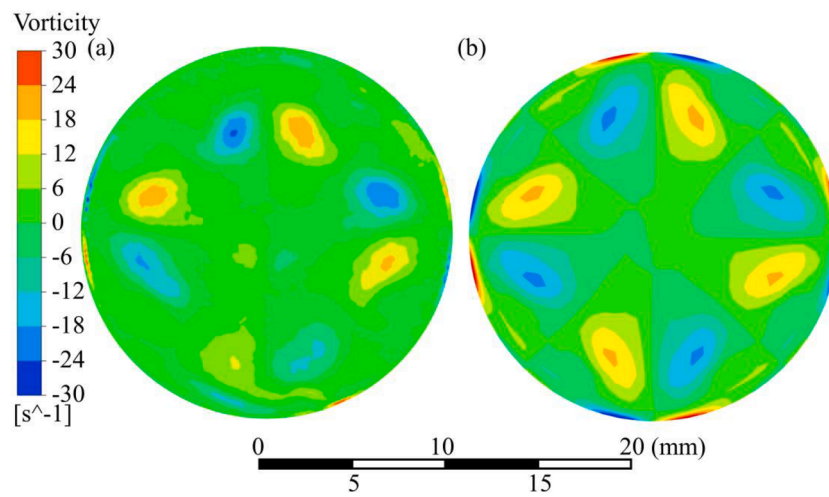

Fig. 14. Vorticity contours for test surface 1: (a) experiment result and (b) simulation result.
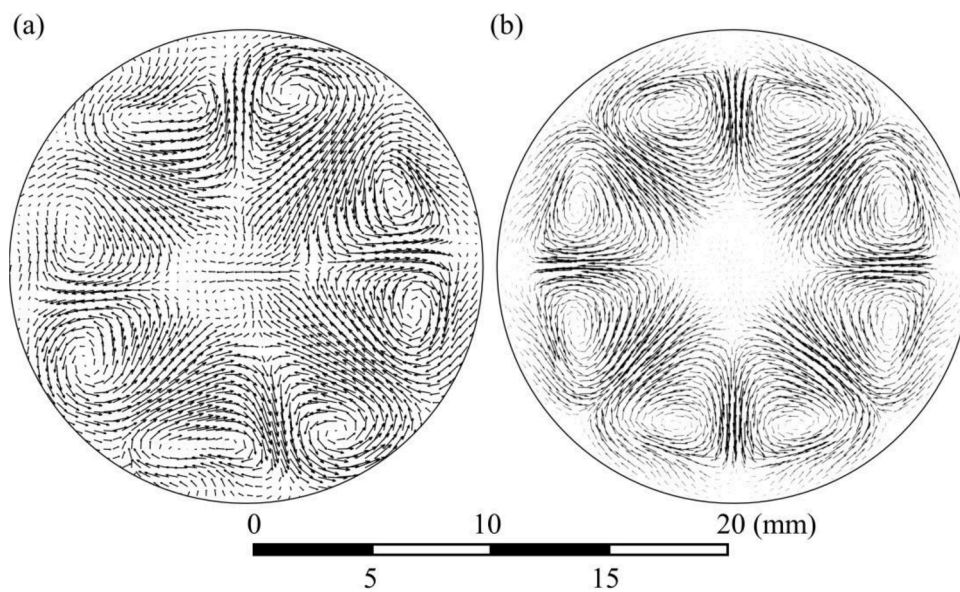
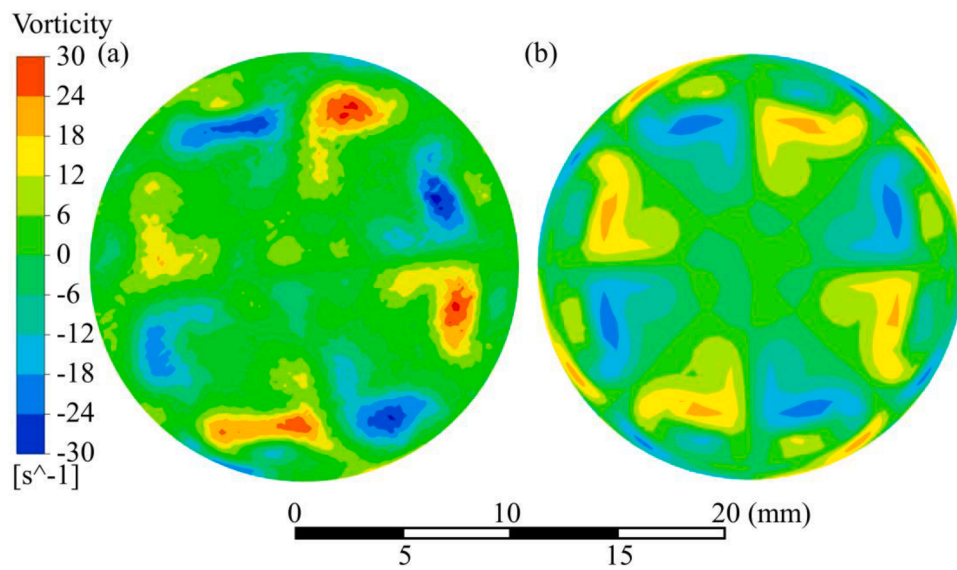**Fig. 15.** Tangential velocity vectors for test surface 2: (a) experiment result and (b) simulation result.

Fig. 16. Vorticity contours for test surface 2: (a) experiment result and (b) simulation result.
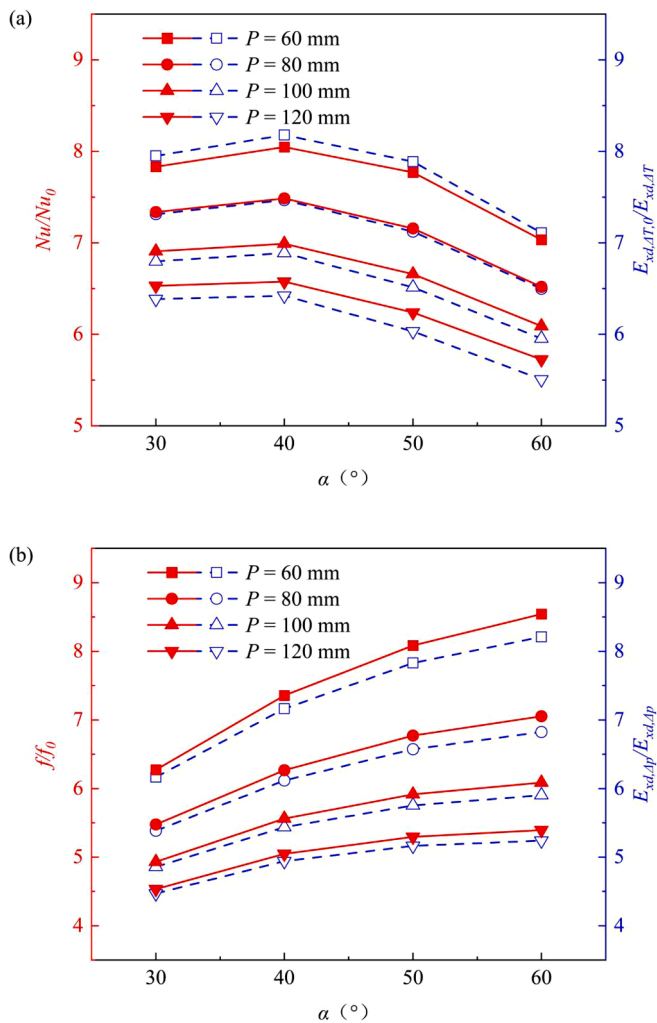
(a)

(b)

Fig. 17. The thermo-hydraulic performance of enhanced tubes varies with slant angle and pitch ($\beta = 40°$, $h = 5.5$ mm): (a) ratios of Nusselt number and exergy destruction of heat transfer and (b) ratios of friction factor and exergy destruction of fluid flow.

areas of high flow resistance. Fig. 18(b) demonstrates the variation pattern of the velocity component u with the slant angle. It is evident that the greater the slant angle, the larger the flow dead zone downstream of the insert. At $\alpha = 60°$, there is a significant backflow phenomenon which causes a great increase in flow resistance. Fig. 17(a) illustrates that the friction factor of the enhanced tube increases as α increases, which is consistent with previous analysis.

Regarding the effect of pitch, it is found that the ratios of the Nusselt number and the friction factor are both negatively correlated with the value of pitch, as shown in Fig. 17. Fig. 19 demonstrates the vortex core regions by method of swirling strength in enhanced tubes under different pitch. It is evident that each set of CBSPs generates the vortex core regions downstream of it and the vortex gradually weakens until the fluid flows over the next set of inserts. Thus, the value of the pitch determines how often the fluid is disturbed and to what extent the heat transfer is enhanced. It is obvious that in an enhanced tube of the same length, the smaller the pitch, the more frequently the fluid is disturbed and the more the heat transfer is enhanced, resulting in an increase of both the Nusselt number and the friction factor.

5.3.2. Effects of bifurcation angle and bifurcation distance

The bifurcation angle and bifurcation distance are important geometric parameters for constructal bifurcation structures. As shown in Fig. 20, with the constant pitch of 80 mm and the constant slant angle of 40°, the thermo-hydraulic performance of enhanced tubes varies with the bifurcation angle under different bifurcation distances. From Fig. 20 (a), it can be observed that as the bifurcation distance increases, the variation pattern of the Nusselt number with increasing bifurcation angle changes from monotonically decreasing to first increasing, then decreasing, and at last to monotonically increasing. It is obvious that the smaller the bifurcation distance and the larger the bifurcation angle, the closer the flow direction of cold water guided by sub semi-pipes tends to be towards the high-temperature regions on the tube wall, resulting in the improved tube wall's temperature uniformity and enhanced heat transfer. However, as shown in Fig. 21, overly large constructal bifurcation structures can also interfere with the multiple longitudinal swirling flows in the center area. When the bifurcation distance is small, as the bifurcation angle increases, vorticity downstream of the insert decreases, which weakens the heat transfer enhancement caused by multiple longitudinal swirling flows, and then the overall heat transfer enhancement may become worse. Fig. 22 demonstrates the variation of the enhanced tube wall's temperature contours with the bifurcation angle for fixed $\alpha = 40°$, $h = 5.0$ mm, and $P = 80$ mm. From the figure, it can be observed that after the fluid flows through a set of CBSPs, the guided cold fluid wash over the tube wall and the wall temperature decreases significantly. As bifurcation angle increases, the cold water is guided more toward the high-temperature regions, resulting in smaller high-temperature areas downstream of the inserts. However, as the fluid flows, the effect of CBSPs guiding the cold water decays, and the enhancement in heat transfer caused by multiple longitudinal swirling flows dominates. CBSPs with larger bifurcation angles generate weaker longitudinal swirling flow, which instead increases overall temperature of the tube wall, resulting in a worse overall heat transfer enhancement. The heat transfer enhancement in the tube is the superposition of these two somewhat conflicting methods, and it is necessary to select the appropriate bifurcation angle and bifurcation distance to achieve better heat transfer performance. As for the friction factor, the head-on area of the insert increases as the bifurcation distance decreases and the bifurcation angle increases, which causes the increasing flow resistance, as shown in Fig. 20(b).

5.3.3. Performance evaluation

With the inlet Reynolds number of 900, the thermo-hydraulic performance of 256 enhanced tubes inserted with different CBSPs are calculated through numerical simulation. The results show that compared to the smooth tube, the Nusselt number of the enhanced tube increased to 5.35–8.16 times, while the friction factor increased to 4.19–9.41 times. The *EEC* reaches a maximum of 1.44, which occurs when $\alpha = 30°$, $\beta = 50°$, $h = 6.0$ mm, $P = 120$ mm. In this case, the Nusselt number of the enhanced tube is 6.52 times that of the smooth tube, and the friction factor is 4.52 times, achieving excellent heat transfer enhancement at the cost of a small increase in flow resistance. From the values of α and P, it can be seen that in the evaluation of CBSPs, *EEC* is more sensitive to the cost of increased resistance. The values of β and h also conform to the previous analysis, that is, when β is large, h cannot be too small, otherwise, the two mechanisms of enhanced heat transfer will conflict. Under this combination of β and h, the heat transfer enhancement caused by CBSPs is good and the head-on area is moderate, so the resistance is not too large.

5.4. Multi-objective optimization

5.4.1. Optimization procedure

Numerical simulation cannot calculate an infinite number of cases with all parameters due to limited arithmetic power. Therefore, to achieve the most suitable performance for different conditions, an optimization on the geometrical parameters of CBSPs is conducted.

The ratios of exergy destruction of fluid flow and heat transfer are selected as optimization objectives, representing the power consump-
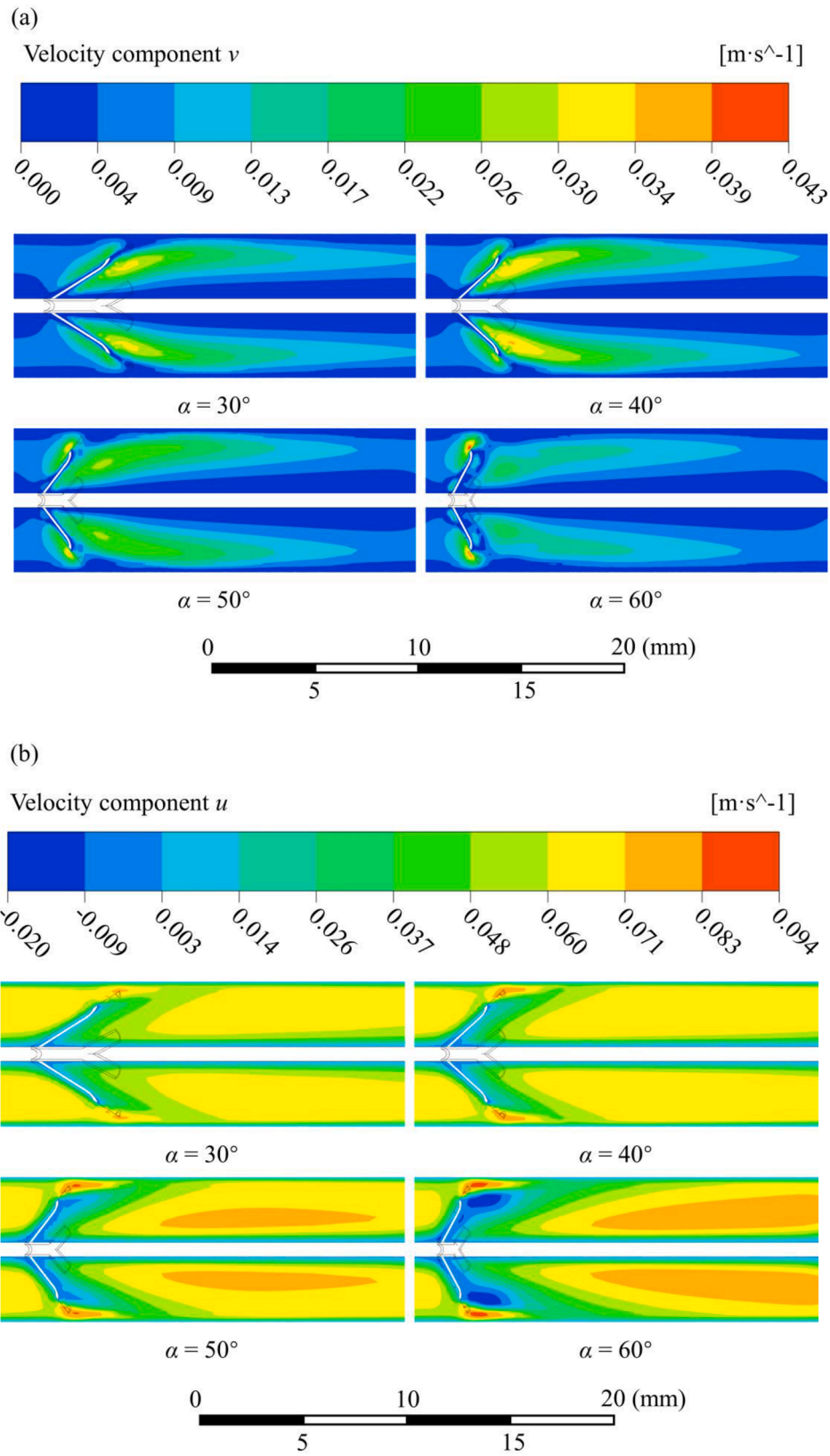
(a)

(b)

Fig. 18. Velocity contours of x-y plane at z=0 in the enhanced tube with different slant angles ($\beta = 40°$, $h = 5.5$ mm, P=80 mm): (a) contours of absolute value of velocity component v and (b) contours of velocity component u.
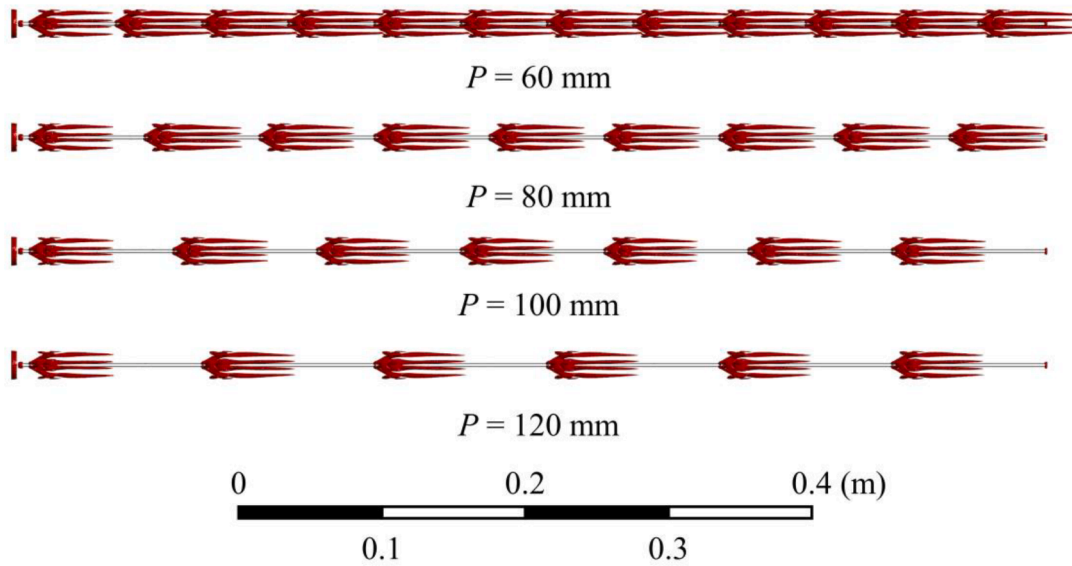
Fig. 19. Vortex core regions by method of swirling strength in the enhanced tube with different pitches ($\alpha = 30°$, $\beta = 40°$, h=5.5 mm).
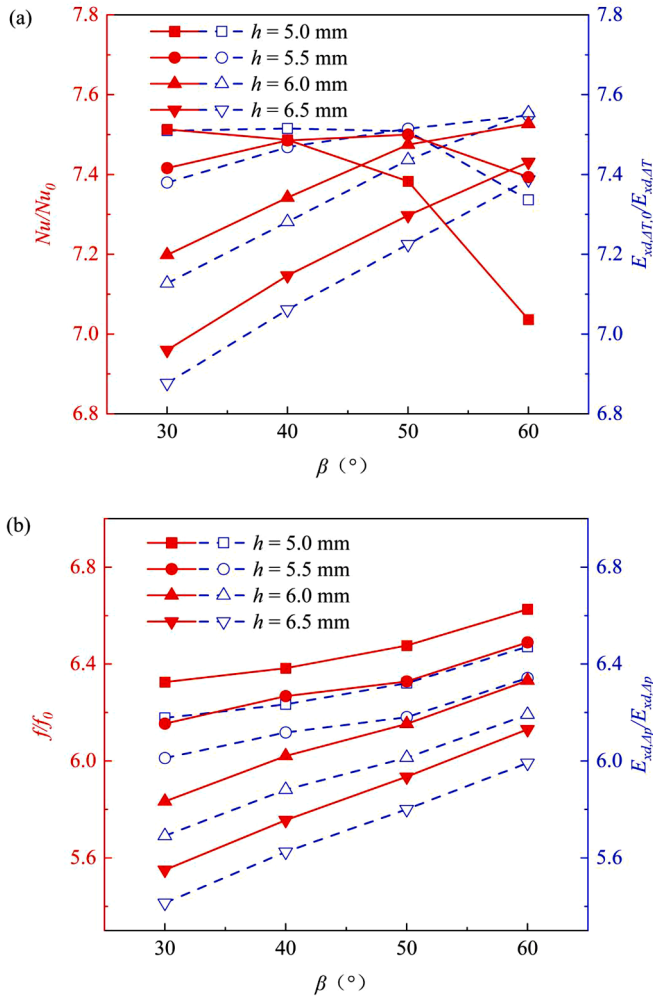

Fig. 20. The thermo-hydraulic performance of enhanced tubes varies with bifurcation angle and bifurcation distance ($\alpha = 40°$, $P = 80$ mm): (a) ratios of Nusselt number and exergy destruction of heat transfer and (b) ratios of friction factor and exergy destruction of fluid flow.

tion caused by pressure drop and the thermal dissipation caused by temperature difference, respectively. They are defined as:

$$Objective_1 = E_{xd,\Delta p} \big/ E_{xd,\Delta p,0} \tag{13}$$

$$Objective_2 = -E_{xd,\Delta T,0} \big/ E_{xd,\Delta T} \tag{14}$$

to meet the objective minimization requirement in the optimization algorithm, the minus sign is added in Eq. (15).

Fig. 23 illustrates the optimization procedure. First, the basic data of cases with four different values for four parameters (256 cases) are obtained by computational fluid dynamics (CFD) simulation. Then, the functional relationship between output and input parameters is fitted using an ANN. Additionally, to obtain the Pareto front, NSGA-II is applied for multi-objective optimization with the trained ANN acting as the objective functions. Finally, based on the requirement, we can select the proper CBSPs design parameters on the Pareto front.

5.4.2. Fitting of the ANN

As shown in Fig. 24, the ANN can be divided into three parts: the input layer, the hidden layer, and the output layer. The input layer has 4 neurons corresponding to the four geometric parameters, while the output layer has 1 neuron corresponding to either $Objective_1$ or $Objective_2$. The number of neurons in the hidden layer is crucial to ANN fitting's accuracy. Thus, an independence test is necessary. Mean square error (*MSE*) and Square of Regression coefficient (R^2) are selected as evaluation indexes, which are defined as:

$$MSE = \frac{1}{N} \sum_{i=1}^{N} \left(X_{i,ANN} - X_{i,CFD} \right)^2 \tag{15}$$

$$R^2 = 1 - \sum_{i=1}^{N} \frac{\left(X_{i,ANN} - X_{i,CFD} \right)^2}{X_{i,CFD}^2} \tag{16}$$

The test results are listed in Table 4, where a smaller *MSE* and a R^2 value close to 1 indicate higher accuracy. It is found that for $Objective_1$, the hidden layer with 18 neurons fits best while for $Objective_2$, the hidden layer with 15 neurons fits best. Fig. 25 shows the relative errors between the results of ANN and CFD. For $Objective_1$ and $Objective_2$, the maximum relative errors are 1.74 % and 1.15 % respectively. Thus, the objective functions obtained by ANN fitting are accurate enough.
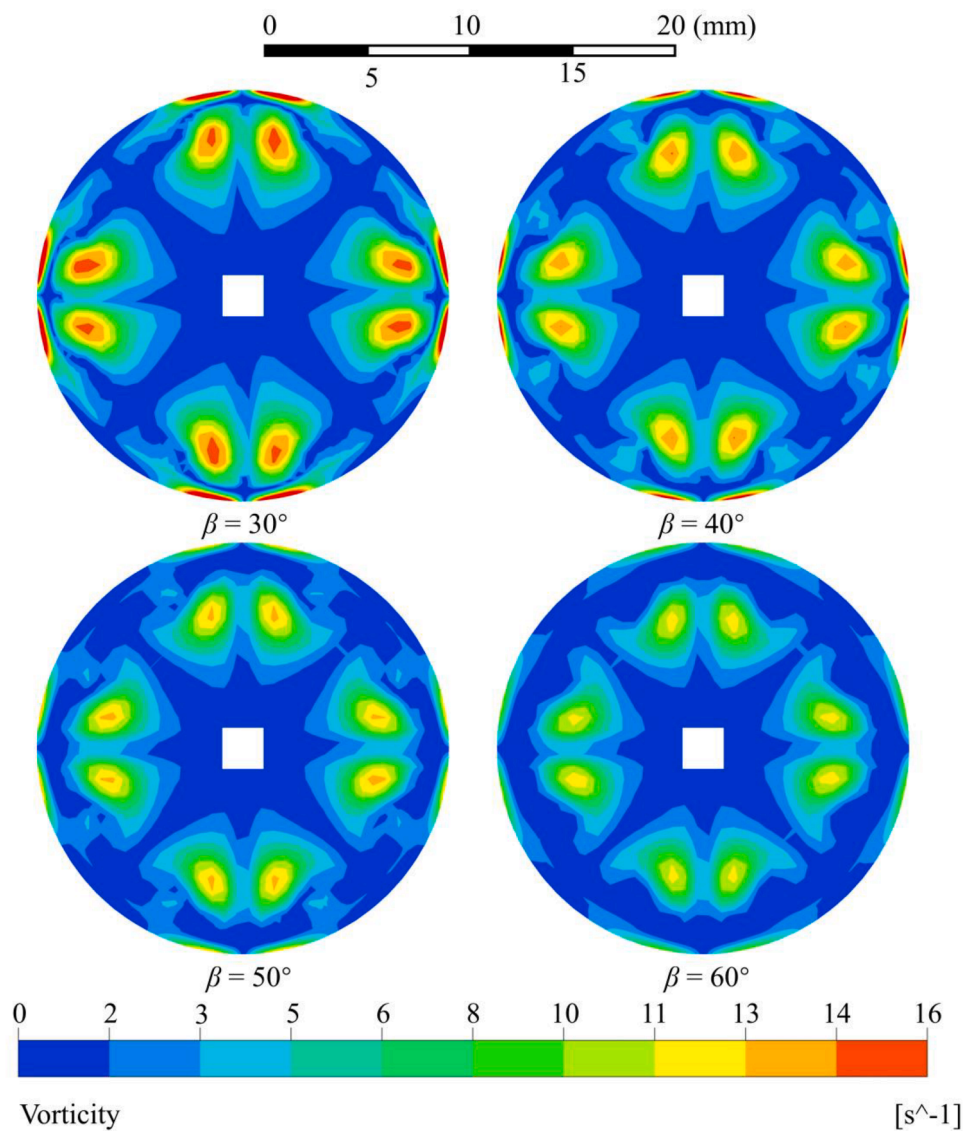
Fig. 21. Contours of absolute value of vorticity on *y-z* plane at *x* = 270 mm in the enhanced tube with different bifurcation angles (*α* = 40°, *h* = 5.0 mm, *P* = 80 mm).
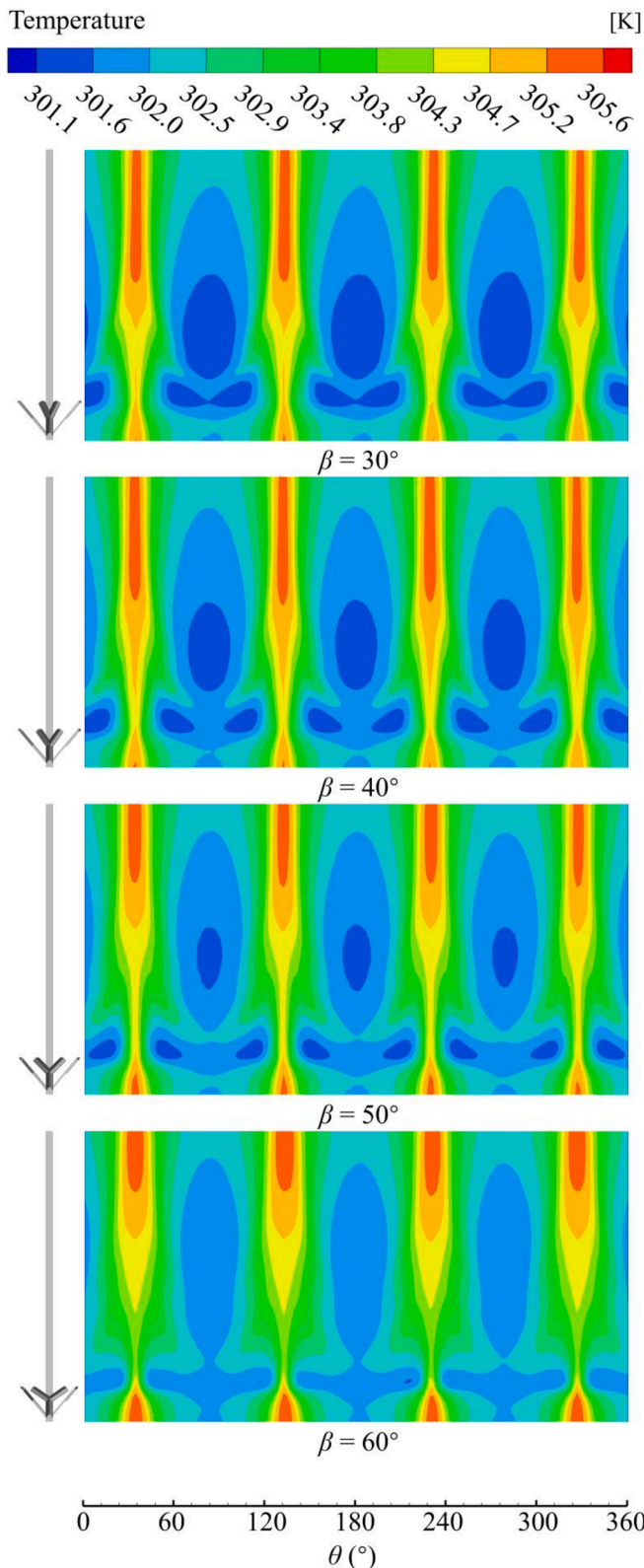
Fig. 22. Temperature contours of tube walls in range of $x = 250$ mm to $x = 330$ mm with different bifurcation angles ($\alpha = 40°$, $h = 5.0$ mm, $P = 80$ mm).

5.4.3. NSGA-II optimization

Multi-objective optimization is conducted using NSGA-II in the commercial software MATLAB with these following settings: the ranges of these four design variables are $5 < h < 6.5$, $60 < P < 120$, $30 < \alpha < 60$, $30 < \beta < 60$; the population size is 500; the max generations are 200; the

Pareto Fraction is 0.2; the Crossover Fraction is 0.8; other parameters are set to default values.

Fig. 26 shows the Pareto front obtained by NSGA-II, where each point represents the minimum heat transfer exergy destruction that can be achieved under a given fluid flow exergy destruction. Thus, each point of this Pareto front is the most beneficial design for a specific situation. For instance, Point A, which has the lowest power consumption, is suitable for situations where savings in pumping power savings are sought, while point B, which has the lowest thermal dissipation, is suitable for situations where heat transfer is enhanced at all costs. However, they also have the highest thermal dissipation and the highest power consumption respectively, which are too extreme for the conventional cases. Therefore, Technique for Order Preference by Similarity to an Ideal Solution (TOPSIS) is used to obtain the Point C, to which the positive ideal has the shortest geometrical distance and the negative ideal has the longest. It is considered a compromise result for conventional situations. The detailed parameters of Point C are $\alpha = 30.19°$, $\beta = 53.56°$, $h = 5.67$ mm and $P = 87.80$ mm. The *EEC* of Point C is 1.35 by CFD simulation, which indicates that excellent comprehensive performance can be obtained based on the principle of exergy destruction minimization according to the second law of thermodynamics.

5.5. Comparison with previous studies

Fig. 27(a)-(c) compares the present work's Nusselt number ratios, friction factor ratios and *EEC* with those of previous works such as alternate clockwise and counter-clockwise twisted tapes [8], porous metal cylinder inserts [12], curved delta wing vortex generators [15], center-connected deflectors [21], multiple conical strips [33], helical screw-tapes [34], and small pipe inserts [35]. It is found that the Nusselt number ratios of this study are at a high level, second only to curved delta wing vortex generators and small pipe inserts under low Reynolds numbers and to alternate clockwise and counter-clockwise twisted tapes under high Reynolds numbers. On the other side, its friction factor ratios are only slightly higher than center-connected deflectors. Therefore, the *EEC* of present work is highest under midstream Reynolds numbers among the listed works.

From a quantitative perspective, the heat transfer enhancement caused by CBSPs surpasses that of earlier inserts such as curved delta wing vortex generators, showing an increase of 5.4 %−17.6 % under high Reynolds numbers. Furthermore, CBSPs can reduce the flow resistance by 80.8 %−82.8 %. The *EEC* can be increased by up to 5.82 times. When compared with longitudinal swirl generators like multiple conical strips, the *EEC* of the enhanced tube can be increased by up to 70.7 %. Even when compared with newer longitudinal swirl generators that guide fluid, such as center-connected deflectors, the *EEC* can still be increased by up to 5.7 % under midstream Reynolds numbers. These underscore the superior comprehensive performance of CBSPs as tube inserts.

6. Conclusion

In this study, a novel type of tube insert, constructal bifurcation semi-pipes, is proposed to improve the tube wall's temperature uniformity. The heat transfer enhancement mechanism of CBSPs under laminar flow is investigated through numerical simulation and experiment. The thermo-hydraulic performance of the enhanced tube is numerically explored. Based on these results, the following conclusions can be drawn:

(I) Through the numerical simulation and Stereo-PIV experiments, it is found that CBSPs do improve the tube wall's temperature uniformity by the method that sub semi-pipes guide part of cold water to wash over the high-temperature regions on the tube wall. This verifies the feasibility of the idea of adding constructal bifurcation structure to a longitudinal swirl generator to improve
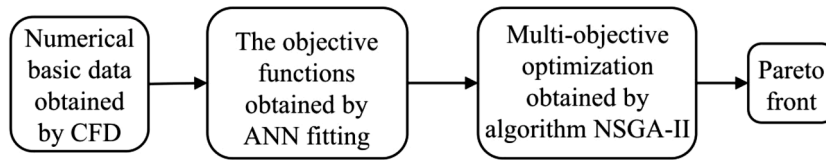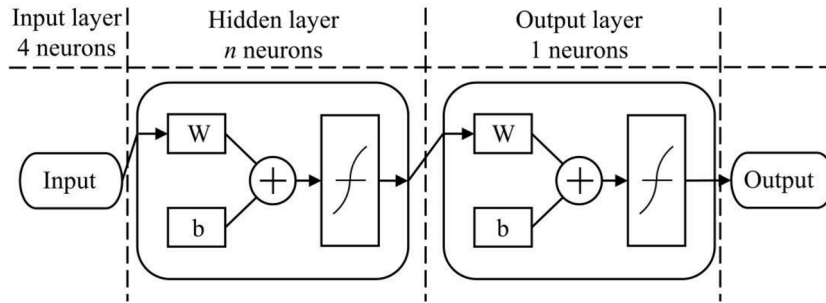
Fig. 23. Optimization flow diagram.

Fig. 24. Structure of neural network.

Table 4
Neuron independence test.

Number of neurons	$net_{\Delta p}$		$net_{\Delta T}$	
	MSE	R^2	MSE	R^2
1	1.29E-03	0.96086	5.12E-03	0.88366
2	6.77E-04	0.97504	2.48E-03	0.94102
3	4.70E-04	0.98341	6.15E-04	0.98630
4	1.92E-04	0.99461	3.55E-04	0.99163
5	1.06E-04	0.99732	1.93E-04	0.99473
6	7.84E-05	0.99783	1.44E-04	0.99634
7	6.52E-05	0.99825	1.35E-04	0.99638
8	7.00E-05	0.99818	8.90E-05	0.99778
9	4.47E-05	0.99880	7.70E-05	0.99795
10	5.57E-05	0.99836	9.01E-05	0.99724
11	6.51E-05	0.99838	6.88E-05	0.99823
12	5.47E-05	0.99844	6.67E-05	0.99818
13	5.42E-05	0.99861	6.38E-05	0.99840
14	6.78E-05	0.99816	6.37E-05	0.99813
15	5.36E-05	0.99844	**5.11E-05**	**0.99868**
16	5.61E-05	0.99858	5.54E-05	0.99840
17	4.45E-05	0.99876	7.31E-05	0.99768
18	**4.21E-05**	**0.99885**	6.33E-05	0.99794
19	5.62E-05	0.99839	5.46E-05	0.99865
20	6.39E-05	0.99841	6.31E-05	0.99823
21	5.55E-05	0.99851	6.65E-05	0.99837
22	7.52E-05	0.99820	6.77E-05	0.99800
23	6.69E-05	0.99823	5.97E-05	0.99850
24	7.03E-05	0.99810	6.28E-05	0.99850
25	5.26E-05	0.99841	6.57E-05	0.99813
26	5.24E-05	0.99853	5.57E-05	0.99844
27	6.96E-05	0.99826	5.85E-05	0.99835
28	6.34E-05	0.99832	6.09E-05	0.99844
29	7.95E-05	0.99798	6.79E-05	0.99827
30	7.62E-05	0.99790	6.51E-05	0.99803

Fig. 25. Comparisons between the results of CFD simulation with the results of ANN fitting: (a) *Objective₁* and (b) *Objective₂*.

the tube wall's temperature uniformity. Moreover, CBSPs also generate multiple longitudinal swirling flows in the circular tube. The sub semi-pipes generate small vortexes while the parent semi-pipes generate large ones downstream of the insert. And as the fluid flows, small vortexes gradually merge with large ones.

(II) Through the parametric study, the effects of slant angle, bifurcation angle, bifurcation distance, and pitch on the thermohydraulic performance of the enhanced tube are investigated. As the slant angle increases, the Nusselt number of the tube first increases and then decreases, reaching a maximum at $\alpha = 40°$ The Nusselt number decreases with increasing pitch. It is important to
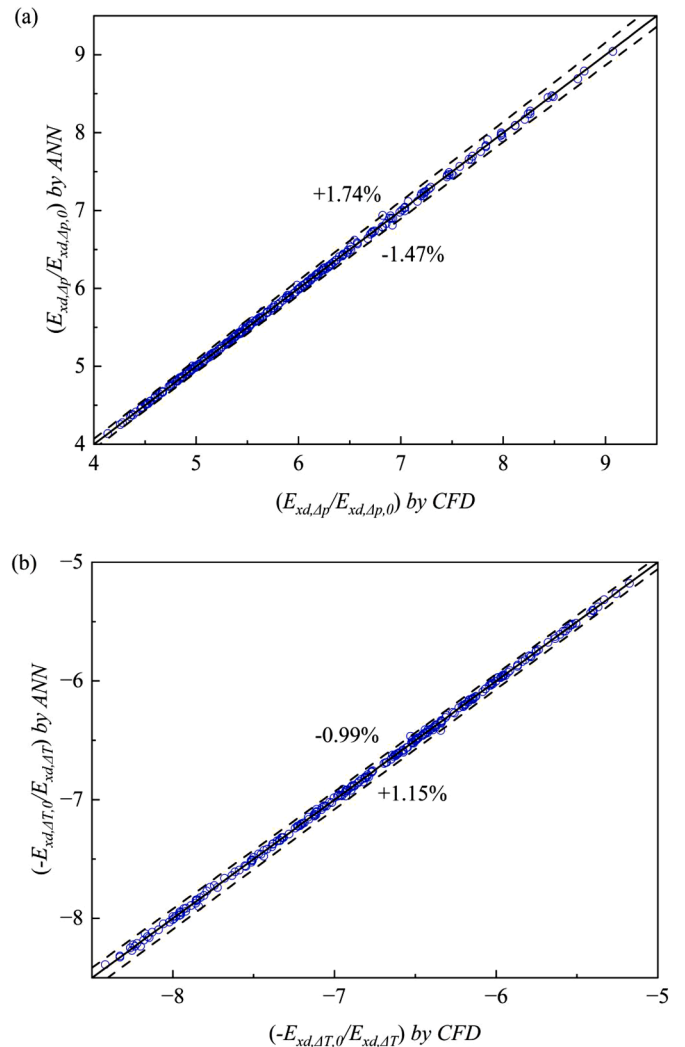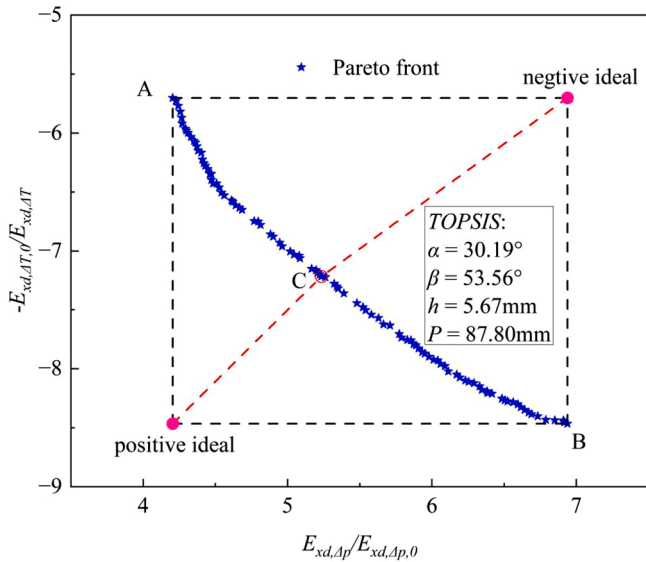
Fig. 26. Pareto front and the compromise result by TOPSIS method.

emphasize that too large constructal bifurcation structures will interfere with the heat transfer enhancement by multiple longitudinal swirling flows. Therefore, as the bifurcation distance increases, the variation pattern of the Nusselt number with increasing bifurcation angle changes from monotonically decreasing to first increasing, then decreasing, and finally becoming monotonically increasing. The friction factor increases with the increase of the slant angle and bifurcation angle, and the decrease of the bifurcation distance and pitch. In the present study, the Nusselt number is increased by 5.35–8.16 times with the friction factor increasing by 4.19–9.41 times compared with the smooth tube. And, the *EEC* is in the range of 0.70–1.44.

(III) According to the principle of exergy destruction minimization, exergy destruction of fluid flow and heat transfer are selected as two objectives for the optimization. ANN is applied to obtain the relationship between the objective functions and variables, and NSGA-II is applied to obtain the Pareto front. The geometric parameters of the compromised point obtained through TOPSIS method are $\alpha = 30.19°$, $\beta = 53.56°$, $h = 5.67$ mm, $P = 87.80$ mm and the corresponding $EEC = 1.35$, which proved that the principle of exergy destruction minimization is effective for design and optimization.

CRediT authorship contribution statement

Qinglin Du: Conceptualization, Data curation, Formal analysis, Investigation, Methodology, Software, Validation, Visualization, Writing – original draft, Writing – review & editing. **Yuhao Zhu:** Methodology, Software. **Peng Liu:** Methodology, Software, Writing – review & editing. **Zhichun Liu:** Funding acquisition, Project administration, Supervision. **Wei Liu:** Conceptualization, Funding acquisition, Project administration, Supervision, Writing – review & editing.

Declaration of Competing Interest

The authors do not have any possible conflicts of interest.
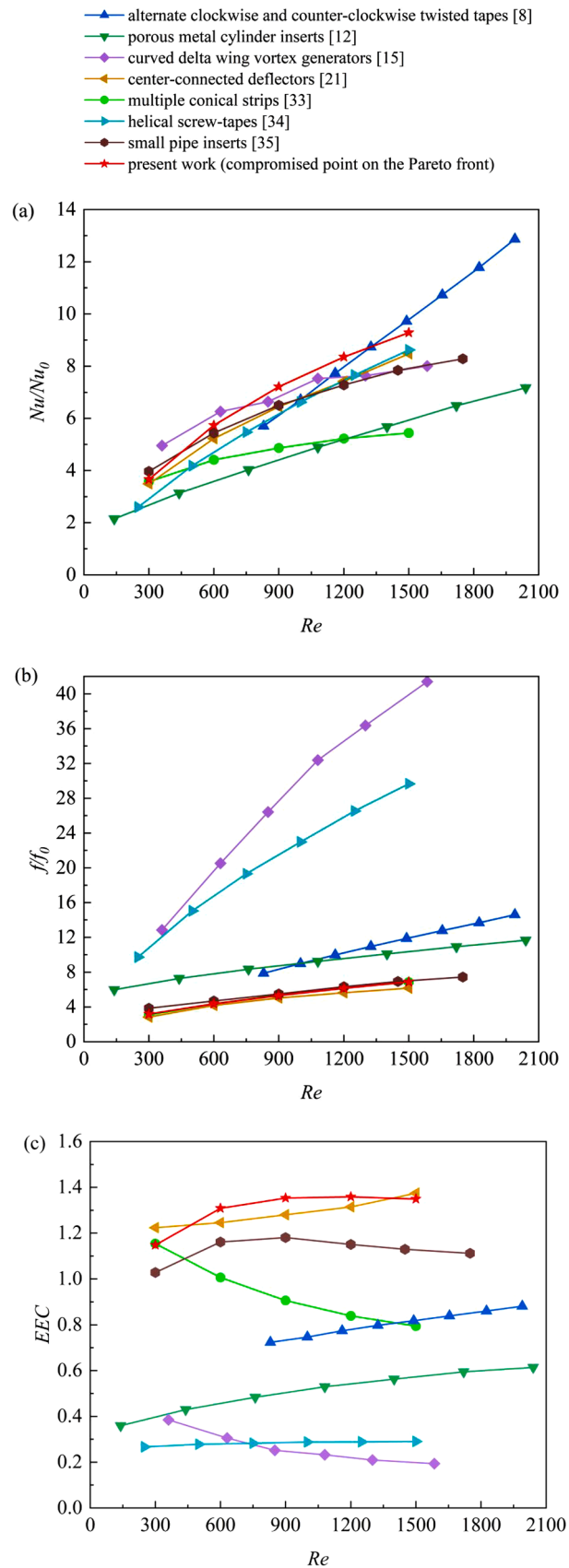
Data availability

Data will be made available on request.

Fig. 27. Comparisons between CBSPs with previous works: (a) Nu/Nu_0, (b) f/f_0, and (c) *EEC*.

Acknowledgements

References

[1] A.E. Bergles, R.M. Manglik, Current progress and new developments in enhanced heat and mass transfer, J. Eng. Heat Transf. 20 (2013) 1–15.

[2] S.A. Marzouk, M.M. Abou Al-Sood, E.M.S. El-Said, M.M. Younes, M.K. El-Fakharany, A comprehensive review of methods of heat transfer enhancement in shell and tube heat exchangers, J. Therm. Anal. Calorim. 148 (2023) 7539–7578.

[3] D. Li, X. Yang, S. Wang, D. Duan, Z. Wan, G. Xia, W. Liu, Experimental research on vibration-enhanced heat transfer of fin-tube vehicle radiator, Appl. Therm. Eng. 180 (2020), 115836.

[4] G. Krishan, K.C. Aw, R.N. Sharma, Synthetic jet impingement heat transfer enhancement – A review, Appl. Therm. Eng. 149 (2019) 1305–1323.

[5] T.M. Liou, S.W. Chang, C.C. Yang, Heat transfer and pressure drop measurements of rotating twin-pass parallelogram ribbed channel, Int. J. Thermal Sci. 79 (2014) 206–219.

[6] C. Thianpong, P. Eiamsa-ard, K. Wongcharee, S. Eiamsa-ard, Compound heat transfer enhancement of a dimpled tube with a twisted tape swirl generator, Int. Commun. Heat Mass Transf 36 (2009) 698–704.

[7] Y. Wang, Y.L. He, Y.G. Lei, J. Zhang, Heat transfer and hydrodynamics analysis of a novel dimpled tube, Exp. Thermal Fluid Sci 34 (2010) 1273–1281.

[8] K. Wongcharee, S. Eiamsa-ard, Friction and heat transfer characteristics of laminar swirl flow through the round tubes inserted with alternate clockwise and counter-clockwise twisted-tapes, Int. Commun. Heat Mass Transf 38 (2011) 348–352.

[9] S.M. Abolarin, M. Everts, J.P. Meyer, Heat transfer and pressure drop characteristics of alternating clockwise and counter clockwise twisted tape inserts in the transitional flow regime, Int. J. Heat Mass Transf. 133 (2019) 203–217.

[10] K. Hata, M. Shibahara, Helically-coiled-wire-induced swirl flow heat transfer and pressure drop in a circular tube under velocities controlled, Int. J. Heat Mass Transf. 204 (2023), 123849.

[11] O. Keklikcioglu, V. Ozceyhan, Heat transfer augmentation in a tube with conical wire coils using a mixture of ethylene glycol/water as a fluid, Int. J. Thermal Sci. 171 (2022), 107204.

[12] S. Huang, Z. Wan, Q. Wang, Y. Tang, X. Yang, Thermo-hydraulic characteristics of laminar flow in a circular tube with porous metal cylinder inserts, Appl. Therm. Eng. 120 (2017) 49–63.

[13] H.J. Xu, Z.G. Qu, W.Q. Tao, Numerical investigation on self-coupling heat transfer in a counter-flow double-pipe heat exchanger filled with metallic foams, Appl. Therm. Eng. 66 (2014) 43–54.

[14] A.H. Altun, H. Nacak, E. Canli, Effects of trapezoidal and twisted trapezoidal tapes on turbulent heat transfer in tubes, Appl. Therm. Eng. 211 (2022), 118386.

[15] P.W. Deshmukh, S.V. Prabhu, R.P. Vedula, Heat transfer enhancement for laminar flow in tubes using curved delta wing vortex generator inserts, Appl. Therm. Eng. 106 (2016) 1415–1426.

[16] P.W. Deshmukh, R.P. Vedula, Heat transfer and friction factor characteristics of turbulent flow through a circular tube fitted with vortex generator inserts, Int. J. Heat Mass Transf. 79 (2014) 551–560.

[17] A. Bejan, A study of entropy generation in fundamental convective heat transfer, J. Heat Transfer 101 (1979) 718–725.

[18] Z.Y. Guo, H.Y. Zhu, X.G. Liang, Entransy—A physical quantity describing heat transfer ability, Int. J. Heat Mass Transf. 50 (2007) 2545–2556.

[19] W. Liu, P. Liu, J.B. Wang, N.B. Zheng, Z.C. Liu, Exergy destruction minimization: a principle to convective heat transfer enhancement, Int. J. Heat Mass Transf. 122 (2018) 11–21.

[20] J. Wang, W. Liu, Z. Liu, The application of exergy destruction minimization in convective heat transfer optimization, Appl. Therm. Eng. 88 (2015) 384–390.

[21] J.Y. Lv, Z.C. Liu, W. Liu, Active design for the tube insert of center-connected deflectors based on the principle of exergy destruction minimization, Int. J. Heat Mass Transf. 150 (2020), 119260.

[22] Z. Sun, K. Zhang, W. Li, Q. Chen, N. Zheng, Investigations of the turbulent thermal-hydraulic performance in circular heat exchanger tubes with multiple rectangular winglet vortex generators, Appl. Therm. Eng. 168 (2020), 114838.

[23] H. Feng, L. Chen, Z. Xie, F. Sun, Constructal design for helm-shaped fin with internal heat sources, Int. J. Heat Mass Transf. 110 (2017) 1–6.

[24] L. Chen, H. Feng, Z. Xie, F. Sun, Thermal efficiency maximization for H- and X-shaped heat exchangers based on constructal theory, Appl. Therm. Eng. 91 (2015) 456–462.

[25] A. Bejan, Street network theory of organization in nature, atr. 30 (1996) 85–107.

[26] A. Bejan, S. Lorente, The constructal law and the evolution of design in nature, Phys. Life Rev. 8 (2011) 209–240.

[27] Z. Hajabdollahi, H. Hajabdollahi, P.F. Fu, Improving the rate of heat transfer and material in the extended surface using multi-objective constructal optimization, Int. J. Heat Mass Transf. 115 (2017) 589–596.

[28] M. Yu, X. Lai, H. Xiao, Z. Liu, W. Liu, A study on flow and heat transfer characteristics of a constructal bifurcation filler in the circular tube, Appl. Therm. Eng. 183 (2021), 116205.

[29] C.W.H. van Doorne, J. Westerweel, Measurement of laminar, transitional and turbulent pipe flow using Stereoscopic-PIV, Exp. Fluids 42 (2007) 259–279.

[30] B. Wieneke, PIV uncertainty quantification from correlation statistics, Meas. Sci. Technol. 26 (2015) 074002.

[31] K. Deb, A. Pratap, S. Agarwal, T. Meyarivan, A fast and elitist multiobjective genetic algorithm: NSGA-II, IEEE Trans. Evol. Computat. 6 (2002) 182–197.

[32] L. Zhang, L. Chen, S. Xia, Y. Ge, C. Wang, H. Feng, Multi-objective optimization for helium-heated reverse water gas shift reactor by using NSGA-II, Int. J. Heat Mass Transf. 148 (2020) 119025.

[33] P. Liu, N. Zheng, F. Shan, Z. Liu, W. Liu, An experimental and numerical study on the laminar heat transfer and flow characteristics of a circular tube fitted with multiple conical strips inserts, Int. J. Heat Mass Transf. 117 (2018) 691–709.

[34] P. Sivashanmugam, S. Suresh, Experimental studies on heat transfer and friction factor characteristics of laminar flow through a circular tube fitted with helical screw-tape inserts, Appl. Therm. Eng. 26 (2006) 1990–1997.

[35] W. Tu, Y. Tang, J. Hu, Q. Wang, L. Lu, Heat transfer and friction characteristics of laminar flow through a circular tube with small pipe inserts, Int. J. Thermal Sci. 96 (2015) 94–101.